Microstructure Characteristics, Texture Evolution and Mechanical Properties of Al–Mg–Si–Mn–xCu Alloys via Extrusion and Heat Treatment

Zulai Li[1,3] · Yingxing Zhang[1,3] · Junlei Zhang[1,3] · Xiang Chen[2] · Suokun Chen[1,3,4] · Lujian Cui[1] · Shengjie Han[1,3]

Abstract

In this work, the impact of extrusion and post-extrusion heat treatment (T6) on the microstructure and mechanical properties of the Al-1.2Mg-0.8Si-0.5Mn alloy with different Cu contents (0, 0.6, 1.3 and 2.0 wt%) was studied. Microstructure characterization showed that all extruded alloys exhibited elongated grain structure with an average grain size of ~ 4.8 μm. The dominant texture components were deformation texture (A*, Copper and P texture), while the proportion of random texture initially increased and then decreased with increasing Cu content. After T6 treatment, the grain size of the four alloys increased significantly, but the growth trend decreased with increasing Cu content, and the textures transformed into recrystallized textures (Cube, A and Goss texture). Tensile testing revealed that the designed T6 alloys with 2.0% Cu content exhibited an excellent strength-ductility balance, i.e., a yield strength of 342.9 MPa, an ultimate tensile strength of 424.8 MPa and an elongation of 15.9%. The enhanced strength was mainly attributed to fine grain strengthening, solid solution strengthening and aging strengthening mechanisms. The superior ductility was due to the pinning effect of fine precipitates and high dislocation accommodation capacity caused by heat treatment.

Zulai Li and Yingxing Zhang have contributed equally to this work and should be considered co-first authors.

✉ Junlei Zhang
983008951@qq.com

✉ Xiang Chen
20230020@huat.edu.cn

1 College of Materials Science and Engineering, Kunming University of Science and Technology, Kunming 650093, China

2 College of Materials Science and Engineering, Hubei University of Automotive Technology, Shiyan 442002, China

3 National and Local Joint Engineering Laboratory of Advanced Metal Solidification Forming and Equipment Technology, Kunming University of Science and Technology, Kunming 650093, China

4 Chinalco International Al Application Engineering Co., Ltd., Beijing 100089, China

1 Introduction

Aluminum (Al) alloys are widely used in the automobiles [1], ships [2] and aerospace [3] due to their high specific strength, light weight, strong machinability and easy welding. Among the various series of Al alloys, the Al–Mg–Si alloy has good corrosion resistance, medium strength, low cost and other characteristics [4–6], making it particularly suitable for industrial applications. Nevertheless, the moderate strength of Al–Mg–Si alloy limits its application in some fields that require higher mechanical properties. Therefore, optimizing the performance of Al–Mg–Si alloy is crucial to expand its industrial application further.

The strengthening mechanism of Al–Mg–Si alloy is based on the formation of numerous precipitates within the matrix during aging. These precipitates effectively hinder dislocation movement, thereby enhancing the strength of the alloy. Consequently, improving the mechanical properties of the alloy involves careful consideration of the type, quantity and size of second phases [7–9]. Based on this concept, researchers have carried out many studies on the performance optimization of Al–Mg–Si alloy. For example, Kuijpers et al.

[10] realized the transition from the flake β-AlFeSi phase to the more stable circular α-Al(FeMn)Si phase in the as-cast microstructure by adjusting the solution temperature. The formation of circular α-Al(FeMn)Si phase could effectively delay the initiation of local cracks during the deformation process, resulting in improved mechanical properties. Xu et al. [11] studied the effect of Mg/Si ratio on Al–Mg-Si series alloys. When the Mg/Si ratio was small (Mg/Si = 1.18, Si = 0.49 wt%), the alloy formed fine and dispersed needle-like phase β-Mg_2Si in the microstructure after rolling and aging treatment. These second phases can significantly improve the strength of the alloy. Ding et al. [12] studied the natural aging and precipitation hardening behavior of Al–Mg–Si alloy with a small addition of Cu at different Mg/Si ratios. The addition of a small amount of Cu (0.6 at.%) led to more Mg_2Si phase and rich Al-Cu-Mg-Si phase at higher Mg/Si ratio and finally exhibited higher peak aging hardness. Rakhmonov et al. [13] studied the effect of Mn content (0%–1.0 wt%) on the microstructure and mechanical properties of the extruded AA6082 alloy. The mechanical properties of the alloy increased first and then decreased with the increase of Mn content. The alloy exhibited peak hardness of 116 HV and yield strength of 335 MPa at 0.5 wt% Mn. The presence of fine-sized and dispersed Al(FeMn)Si phase provided the best mechanical properties. However, excessive Mn content caused coarsening of precipitates, leading to reduced hardness and yield strength. Ding et al. [14] studied the effect of Zn on the aging behavior of Al-0.99Mg-0.54Si alloy. Increasing the proportion of Zn element shortened the peak aging time increased the peak hardness. However, elevated aging temperature caused the decrease of hardness due to the melting back of $MgZn_2$ into the matrix. Wen et al. [15] introduced 0.5 wt% Ag into Al–Mg–Si alloy. The Ag element entered the Mg–Si clusters during early aging stage, refining the cluster and promoting the formation of other clusters. Ultimately, the precipitates became smaller in size, but increased in number, which significantly improved the hardness of the alloy.

In addition, many studies have been conducted on the optimization of the mechanical properties of Al–Mg–Si alloy by adding rare earth elements. For example, Ding et al. [16] added 0.1 wt% Y and 0.2 wt% Al-Ti-B to 6063 alloy. After subjecting to T6 treatment, the existence of Y element inhibited the precipitation of Mg_2Si, which significantly improved the plasticity of the alloy. The addition of Al-Ti-B played a role in pinning dislocations and refining the grains, thereby significantly improving the strength of the as-cast microstructure, with limited contribution to plasticity. Wang et al. [17] investigated the aging strengthening mechanism of Al–Mg–Si alloy hot-rolled sheets under the influence of Sc. In the early stage of aging, the existence of Sc atom dramatically hindered the annihilation of vacancies, resulting in increased density of the precipitated phases and

improved peak aging hardness. Jiang et al. [18] studied the effect of trace La element on the aging behavior of rolled Al-0.6Mg-0.6Si alloy. They pointed out that the addition of 0.08% La element reduced the undercooling of α-Al and Mg_2Si nucleation, which in turn played a role in refining the α-Al matrix and (Mg, Si) phase. This ultimately achieved an increase in alloy strength with a small effect on elongation.

The above numerous cases show that the mechanical properties of Al–Mg–Si alloy can be improved by regulating the alloy composition. In view of the production cost and effectiveness, selecting appropriate strengthening elements is of great significance to expand the industrial application of Al–Mg–Si alloy. Cu, as a traditional strengthening element, has been extensively studied due to its relatively low price and effective strengthening effect [19, 20]. However, the current research mainly focuses on the mechanical properties of Al–Mg–Si alloy with trace Cu addition (0–0.5 wt%), and there is a lack of research on higher Cu contents (0.5–2.0 wt%). Moreover, existing research on the microstructure regulation and mechanical behavior of Al–Mg–Si–Cu alloy primarily involves the as-cast or as-rolled state, with limited research on the effect of extrusion on the microstructure, precipitated phase and mechanical properties of Al–Mg–Si–Cu alloy. Extrusion, as a forming process, subjects the alloy to a three-directional hydrostatic pressure during sheet forming, effectively avoiding edge crack problems associated with rolling and causing microstructure characteristics different from the rolled state.

Based on the above considerations, this work focused on the microstructure and mechanical properties of extruded Al–Mg–Si–Mn alloy with medium Cu content (0.6–2.0 wt%). Additionally, post-extrusion heat treatment (T6) was applied to further enhance the mechanical properties of Al–Mg–Si–Mn alloy. The results displayed significant improvements in strength by adding medium content of Cu. In addition, the microstructure characteristics using SEM, XRD, EBSD and TEM techniques provides insight into the relationship between microstructure and mechanical properties. This work provides a new perspective for the performance optimization of Al–Mg–Si alloy.

2 Experimental

The experimental alloys were obtained by vacuum melting method. The raw materials for smelting were high purity Al (99.85 wt%), high purity Mg (99.9 wt%) and intermediate alloys of Al-10 wt% Mn, Al-20 wt% Si and Al-50 wt% Cu. Four alloys with Cu content ranging from 0.0 wt% to 2.0 wt% were obtained by adjusting the ratios of the above pure Al, Mg ingots and intermediate alloys. After melting, these alloys were cast to obtain ingots. X-ray fluorescence spectrometer (XRF) was used to analyze the elements of

four kinds of ingots after smelting; the detailed results are given in Table 1. Subsequently, the obtained four alloys were first cut into cuboids of $16.5 \times 16.5 \times 35$ mm^3 using wire cutting and then were homogenized at 540 °C [21] for 2 h. The treated ingots were cooled to room temperature by water quenching [22]. After surface treatment, the samples were subjected to extrusion at 400 °C with an extrusion ratio of 12.8:1, and the final sheet thickness was 1.5 mm. The extruded samples were then treated with T6, i.e., solid solution at 540 °C for 2 h followed by aging at 170 °C for 8 h. According to the Cu content, four kinds of extruded samples were named ES-0Cu, ES-0.6Cu, ES-1.3Cu and ES-2.0Cu, respectively. Similarly, the T6-treated samples were named SA-0Cu, SA-0.6Cu, SA-1.3Cu and SA-2.0Cu,

respectively. The above relevant steps are displayed in Fig. 1.

Samples for optical microscope (OM, Carl ZEISS-Axio Imager) and scanning electron microscopy (SEM, VEGA-3SBH) observation were firstly polished to 4000# with water abrasive paper and then were etched using Keller Reagent (95 mL H$_2$O, 2.5 mL HNO$_3$, 1.5 mL HCl, 1.0 mL HF) for as-cast sample and Week's Reagent (100 mL H$_2$O, 4g KMnO$_4$, 1g NaOH) for extruded samples. X-ray diffraction (XRD, Ultima IV) was used to analyze the phase of the samples. For electron backscatter diffraction (EBSD, Nova-Nan0 SEM450) analysis, the samples were further electro-polished at -20 °C using a 7 vol.% HClO$_4$ alcohol solution with a voltage of 20 V for 20 s.

Table 1 Chemical compositions of the four kinds of alloys in this study (wt%)

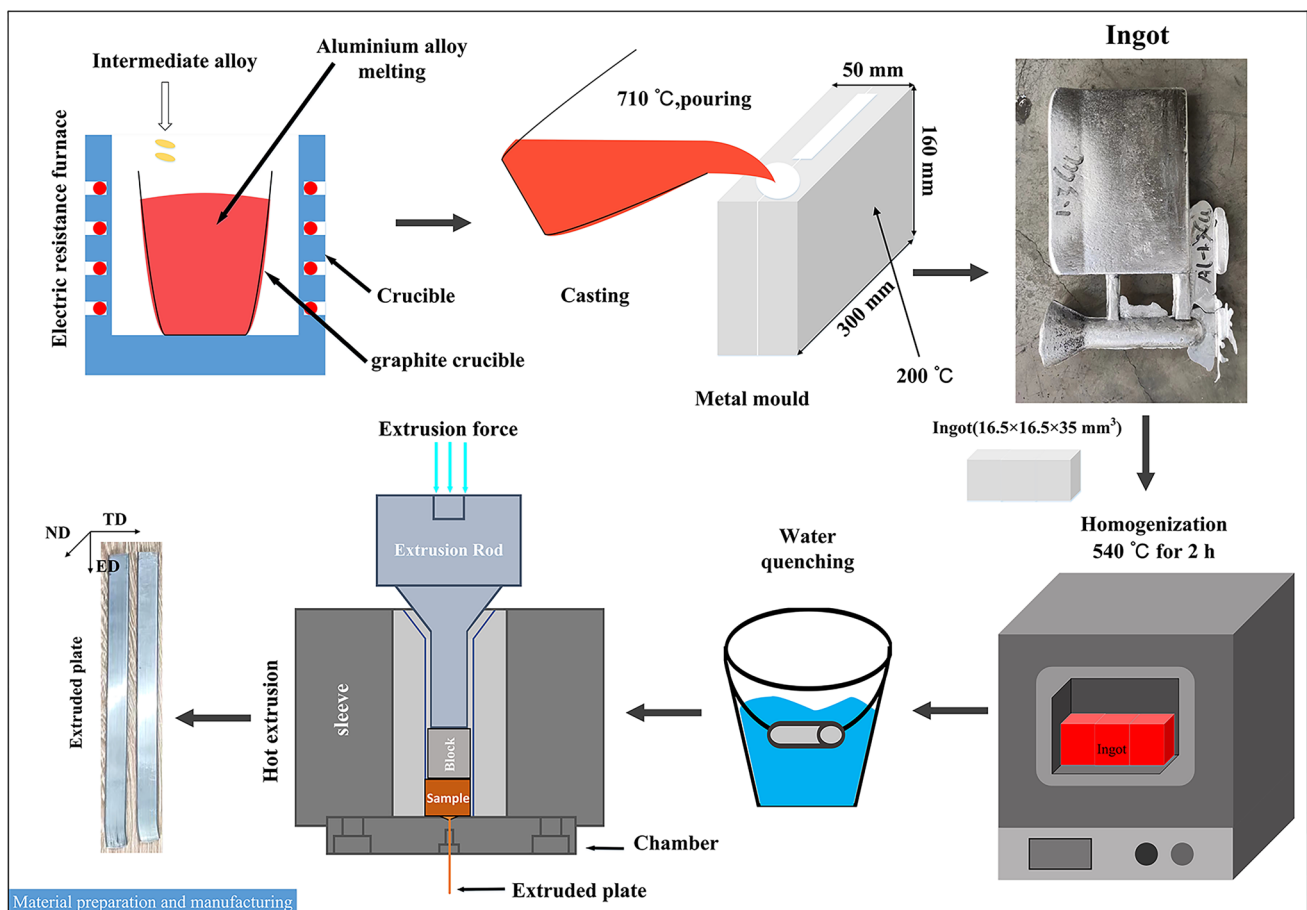| Samples state	Mg	Si	Mn	Cu	Fe	Al
1	1.23	0.85	0.46	–	0.08	Bal.
2	1.21	0.89	0.41	0.58	0.08	Bal.
3	1.26	0.86	0.42	1.33	0.11	Bal.
4	1.24	0.84	0.43	1.98	0.10	Bal.

Fig. 1 Schematic diagram of Al–Mg-Si-Mn-Cu alloy melting preparation and extrusion process

The acquired EBSD data were processed on Channel 5 software. Samples for transmission electron microscopy (TEM, Tecnai G2 TF30) analysis were polished to 50 μm and then stamped to obtain a disc with a diameter of 3 mm. The disc was electrolytically thinned by double-jet electrolysis at -25 °C using an electrolyte solution consisting of nitric acid and methanol in volume ration of 1:3. Finally, TEM observations were performed at 200 kV. The Vickers hardness test was carried out on the ED-ND plane using a Shimadzu HMV-G20 Vickers hardness tester with a load of 300 N and a dwell time of 15 s. The topography characteristics of hardness points were recorded using Rtec UP-Lambda three-dimensional topography instrument. Tensile tests were carried out on dog-bone-type flat samples with dimensions of $25 \times 4 \times 1.5$ mm^3 at a speed of 0.75 mm/min. Tensile tests under each condition were performed three times. Finally, SEM was used to examine the fracture morphology of the tensile samples.

3 Results

3.1 Microstructural Characterization

Figure 2 displays the OM diagram of the four kinds of alloys in the as-cast state. It can be seen that these alloys presented typical as-cast microstructure characteristics. Due to the rapid cooling rate during the casting process, serious dendrite segregation was observed near the grain boundaries, which had been reported in early study [23]. The microstructure of alloy without Cu addition consisted mainly of α-Al and irregular eutectic compounds. In addition to the distribution of eutectic compounds along the grain boundaries, a small amount of distribution inside the grains was also observed. However, after adding Cu, the segregation of the microstructure was further aggravated. In addition to the distribution along the grain boundaries, the number of eutectic compounds within the grains increased. The formation of intragranular compounds in α-Al grains played a segmented role, which made the microstructure show a refinement characteristic. A comparison Fig. 2b, c and d revealed an
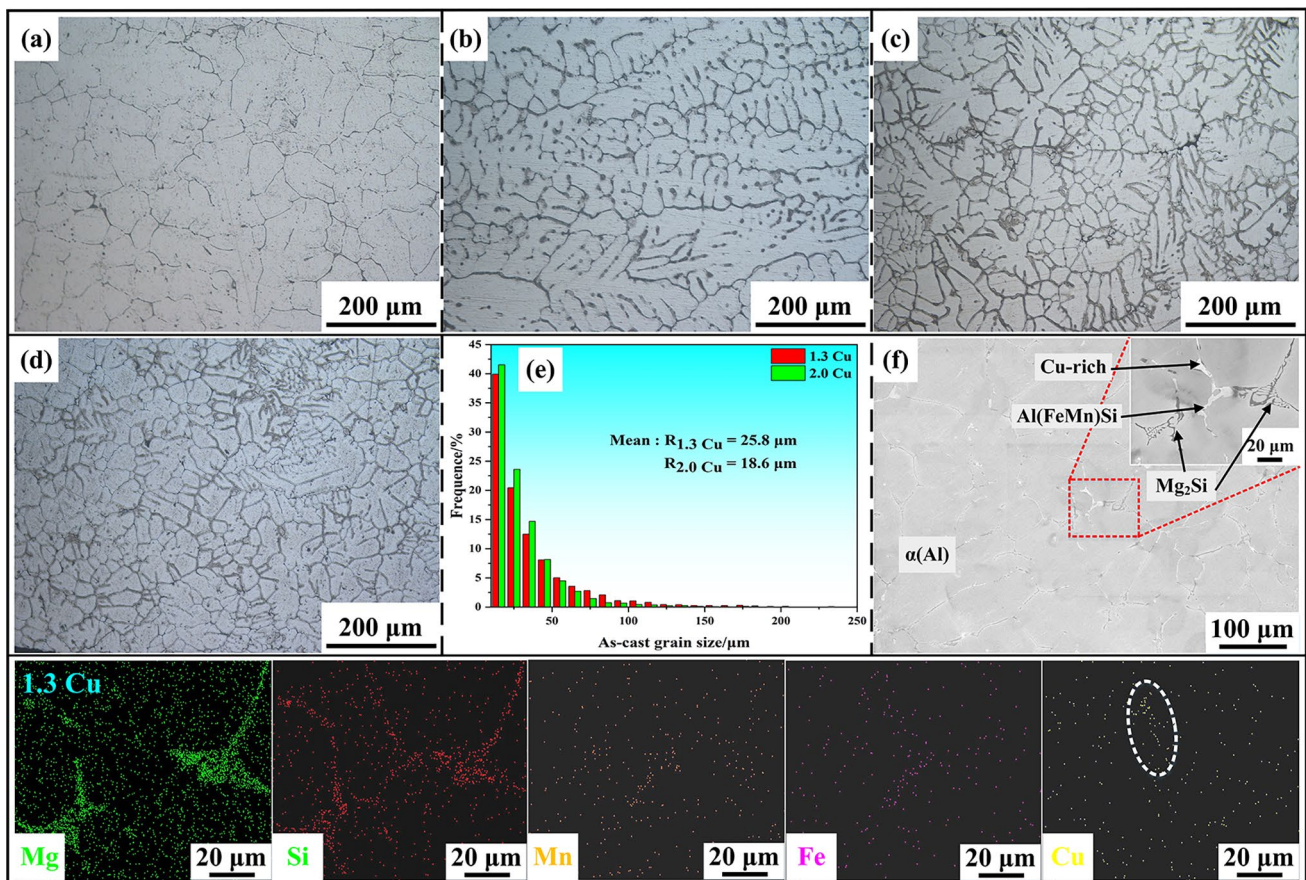

Fig. 2 As-cast metallographic diagram of four alloys: **a** 0Cu; **b** 0.6Cu; **c** 1.3Cu; **d** 2.0Cu; **e** grain size statistics for 1.3Cu and 2.0Cu; **f** SEM for 1.3Cu and EDS for selected portions of the area

increasing refinement trend in the microstructure. This may be attributed to the fact that the addition of Cu intensified the microstructure segregation within the grains, leading to the unbalanced crystallization of the microstructure. Statistics on grain size showed an average grain size of 25.8 μm for the 1.3Cu alloy, while the average grain size for the 2.0Cu alloy was 18.6 μm. Energy disperse spectroscopy (EDS) analysis of selected areas of 1.3Cu alloy (Fig. 2f) revealed areas of Cu aggregation (white ovals in Fig. 3f). Combined with the existing research findings [24–26], the elongated eutectic structure was identified as Mg_2Si and the coarse rod-like eutectic structure as Al(FeMn)Si. Meanwhile, the white compound was identified as a Cu-rich phase, with its specific composition to be further explored in subsequent studies.

After homogenization, the above four alloys were extruded. The changes in the grain characteristics of the alloys can be apparently seen from the inverse pole figure (IPF) diagram in Fig. 3. The microstructures of the four extruded sheets all presented a fibrous distribution along the ED (Fig. 3a–d), which is a common feature of deformed Al alloys [5, 6]. In the case of the ES-0Cu sample, only a small amount of the grains was red (001) orientation, while most of the grains exhibited pink (113) and cyan (101) orientations located between (001) and (111). In the ES-0.6Cu sample, there was no significant change in grain orientation,

but the proportion of cyan (101) orientation grains appeared to decrease, favoring the pink (113) orientation grains. In ES-1.3Cu sample, a larger proportion of grains displayed the cyan (101) orientation, with only a small proportion showing the pink orientation. For ES-2.0Cu alloy, the grains were primarily composed of lavender (232) and pink orientation grains, with a small amount of cyan (101) and (001) grains. Additionally, further observation of the internal orientation in the grains for the four alloys revealed that the phenomenon of inconsistent orientation still existed inside some coarse deformed grains. This phenomenon may be due to the larger grain size after homogenization treatment. These coarse grains experienced uneven forces between internal regions during the deformation process, inducing differences in deformation activities such as rotation and sliding within the grain microintervals, thereby causing gradient changes in grain orientation [27]. Additionally, high-temperature recovery and the nucleation and growth of grains inevitably caused changes in grain orientation.

IPF diagrams of the four T6-treated alloys are given in Fig. 3e–h. The grains of the four alloys exhibited a trend of widening in the ND direction, and the grain was significantly coarsened. However, despite the grain coarsening, the elongated grain structure along the ED direction was still evident. Comparing the four alloys, it was found that adding Cu
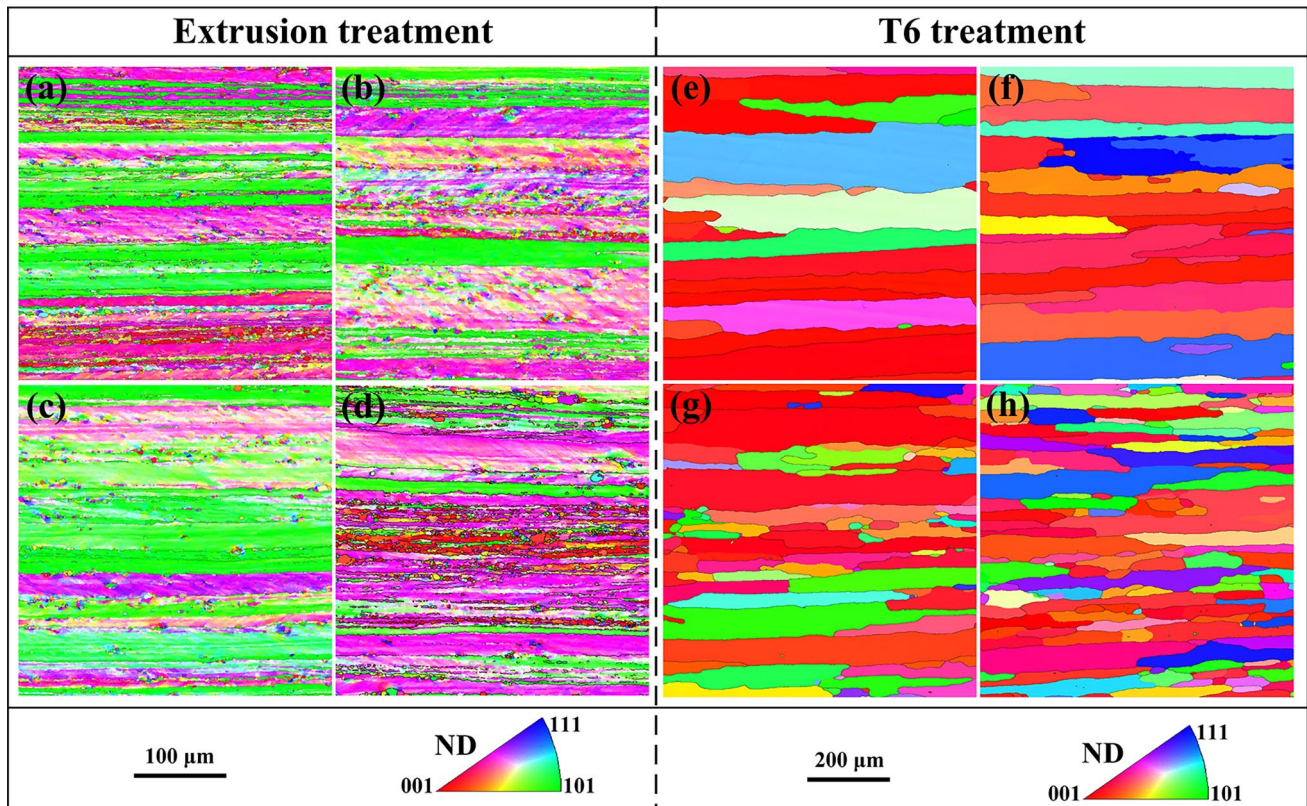

Fig. 3 IPF maps (in ND): **a** ES-0Cu; **b** ES-0.6Cu; **c** ES-1.3Cu; **d** ES-2.0Cu; **e** SA-0Cu; **f** SA-0.6Cu; **g** SA-1.3Cu; **h** SA-2.0Cu

on the basis of Al–Mg–Si–Mn alloy had a significantly grain refinement effect. Meanwhile, the T6-treated alloys revealed significant changes in grain orientation after solution at high temperature compared to the extruded sheets. The internal grain orientation in all four T6-treated alloys tended to be consistent, with an increased proportion of grains exhibiting a red (001) orientation. The SA-0Cu (Fig. 3e) alloy was mainly composed of red (001) orientation, cyan (101) orientation, purple (113) orientation and yellow (214) orientation. With the addition of Cu, the SA-0.6Cu sample displayed the presence of yellow grains with (214) orientation, and the proportion of these grains increased in SA-1.3Cu and SA-2.0Cu samples. Although the grain orientation within the microstructure of the four T6-treated alloys presented diversify, there was a tendency toward greater consistency in grain orientation. The discrepancies in texture distribution and intensity caused by the differences in grain orientation will be further discussed in the subsequent pole diagram analysis.

Grain size is one of the important factors affecting the mechanical properties of metals. To better demonstrate the differences in grain size among the above alloys, the method of "Circle Equivalency Diameter" in Channel5 (also seen commonly in metals [28]) was used to statistically analyze the grain size distribution of the four sheets, as depicted in Fig. 4. The redder the grain color, the larger the grain size. It can be seen that the grain color of the four extruded alloys (Fig. 4a–d) was mainly blue and light green, indicating that their grains were smaller. Meanwhile, Fig. 4a–d displays the average equivalent circle diameter of the four extruded sheets, which were 4.97 μm, 4.60 μm, 4.77 μm and 4.57 μm in sequence. The results indicated that the differences in grain sizes of the four extruded alloys were relatively small.

The T6 treatment involves both the solution and aging treatments, where the solution treatment is the dominant factor causing grain coarsening in T6-state plates, while the aging process is dominated by the precipitation of phases with limited contribution to grain growth [29]. After T6 treatment, the grain color of the four alloys tended to be yellow and red. SA-0Cu covered not only the light blue grains with a grain size of about 50 μm, but also the bluish-yellow grains with a grain size of 150–250 μm and some red grains with a grain size of about 380 μm. The grain of the SA-0.6Cu alloy was refined, and the number of grains with a grain size near 30 μm increased. As the Cu content continued to increase, finer equiaxed grains appeared in the microstructure. The grain refinement phenomenon was most prominent in SA-2.0Cu alloy. The average grain sizes of the four alloys were 146.02 μm, 112.38 μm, 59.80 μm and 55.60 μm, respectively. When the Cu element was added to the
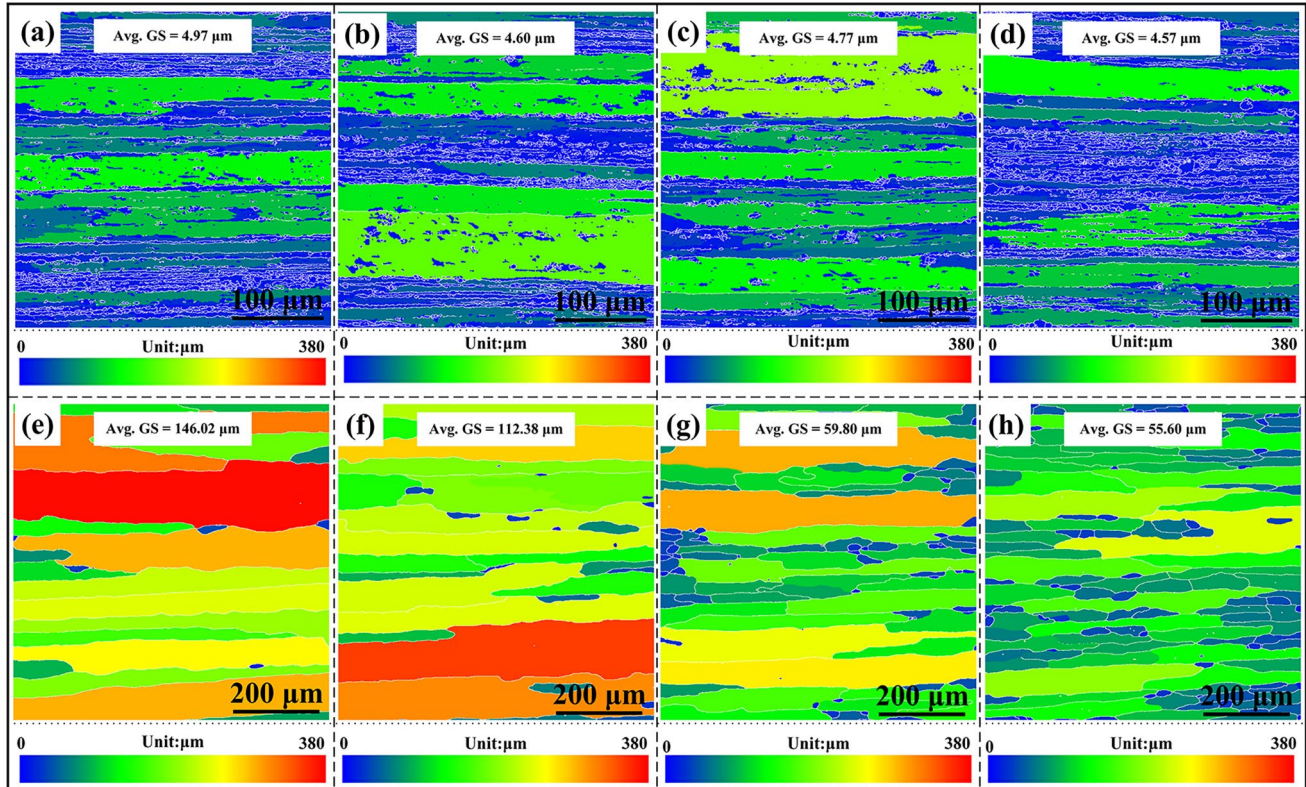

Fig. 4 Grain size distribution maps: **a** ES-0Cu; **b** ES-0.6Cu; **c** ES-1.3Cu; **d** ES-2.0Cu; **e** SA-0Cu; **f** SA-0.6Cu; **g** SA-1.3Cu; **h** SA-2.0Cu

matrix, some Cu element dissolved into the matrix and hindered the movement of grain boundaries. The other part of the Cu element precipitated and formed a fine second phase, which further inhibited the growth of grains [30]. Therefore, adding Cu element to the alloy resulted in grain refinement, and this effect became more apparent with increasing Cu content.

The IPF diagram demonstrated that there were some differences in the grain orientation of the alloy with the change of the sheet state and alloy elements, and the difference in grain orientation led to variations in the texture of the alloy, so the pole figure of the alloys was calculated, as indicated in Fig. 5. The results demonstrated that the texture intensity of the four extruded alloys (Fig. 5a–d) inclined firstly and then

declined, presenting a W-shaped texture distribution feature ((001) plane). The W-type characteristics were the most obvious in ES-0Cu alloy, but this phenomenon presented a decreasing trend with the addition of Cu. The maximum pole density of the ES-0Cu alloy was 9.53. However, the pole density of ES-0.6Cu and ES-1.3Cu increased, possibly due to the enhanced strength of this type of texture. For ES-2.0Cu alloy, its maximum pole density dropped to 11.44, and the change of texture intensity may be caused by the change of texture type. After T6 treatment, the maximum texture density of the four alloy sheets appeared an overall decreasing trend compared with the extruded alloy. With the increase of Cu content, the texture density of the four alloys gradually decreased, with maximum polar densities
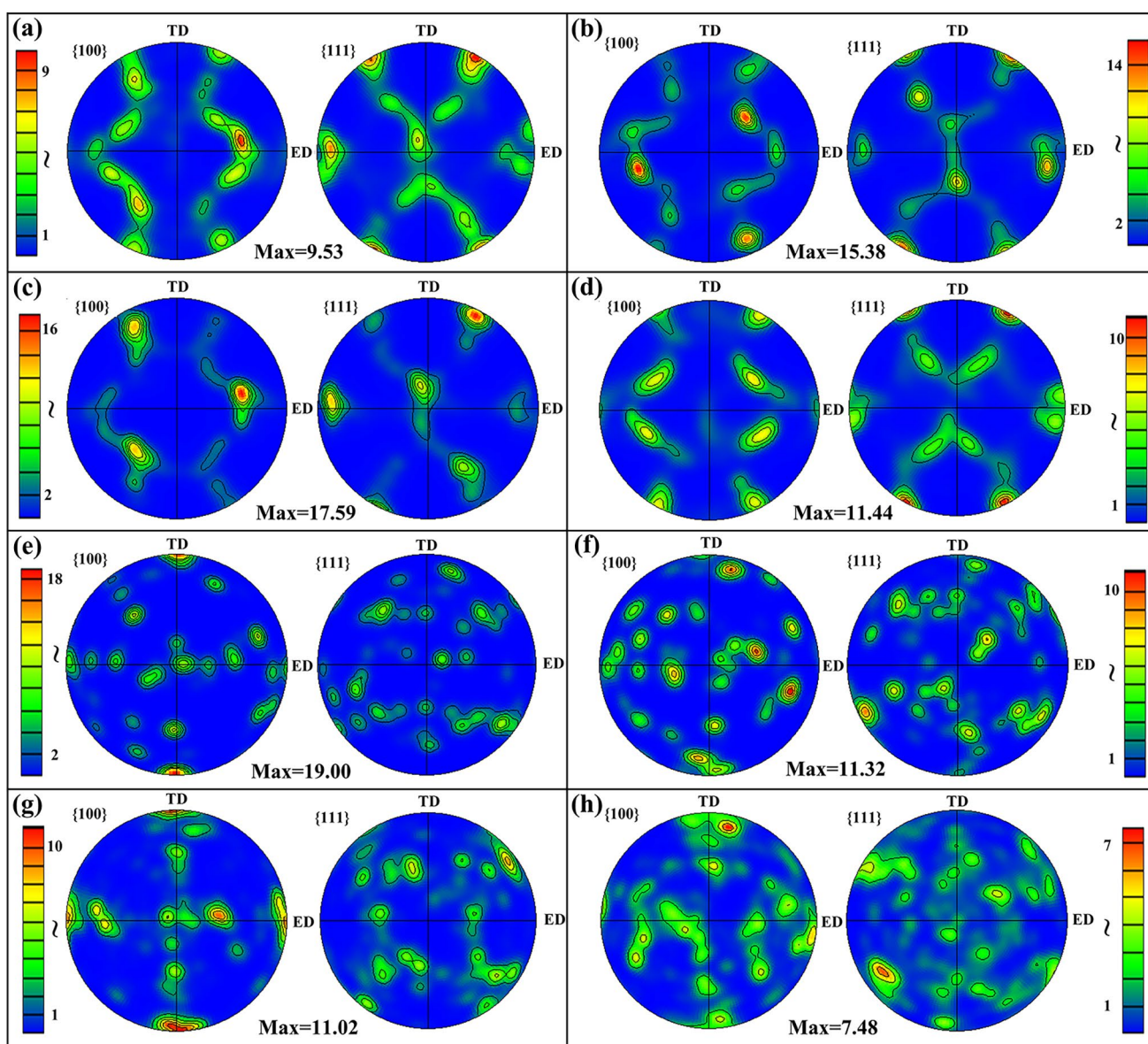

Fig. 5 Diagram of PF: **a** ES-0Cu; **b** ES-0.6Cu; **c** ES-1.3Cu; **d** ES-2.0Cu; **e** SA-0Cu; **f** SA-0.6Cu; **g** SA-1.3Cu; **h** SA-2.0Cu

of 19.00, 11.32, 11.02 and 7.48, respectively. The texture characteristics and composition changes of the sheets will be further explained and analyzed in the discussion section.

3.2 SEM and XRD

After extrusion and T6-treated treatment, punctate particles were observed in all four alloys. In order to determine the morphology and composition of the above-mentioned point-like particles (Fig. 3), the microstructures of the four alloys after extrusion and T6-treated treatment were analyzed by SEM and EDS, as presented in Figs. 6 and 7. Based on the results of Fig. 6, a certain amount of black and white precipitated particles appeared in the four alloy microstructures and were distributed in the matrix in the form of star chain along the ED direction. With the addition of Cu, the number of chain-like precipitated particles indicated an increasing trend, and the size of precipitated phase also increased. During the extrusion process, the grain experienced severe

plastic deformation and produced a lot of dislocations and sub-grain boundaries. These defects could transport the solution elements in the matrix to the locations with high dislocation density at a high speed, leading to higher saturation in a short time [31]. This provided a large number of favorable nucleation sites for the precipitation of the second phase, thereby promoting the precipitation of elements and the formation of second phase. The precipitated phase in the microstructure exhibited a strong pinning effect on the grain boundary and sub-grain boundary, thereby inhibiting grain growth. Figure 7 gives the SEM image of four T6-treated alloys, where the black and white precipitated particles were evenly dispersed. The number and size of particles in SA-0Cu did not change much compared with ES-0Cu, while the number and size of particles in the other three alloys decreased compared with those after extrusion treatment. Taking 1.3Cu and 2.0Cu alloys as examples, EDS surface scanning was carried out to judge the distribution of Cu element in the alloy. The results indicated that the larger phases
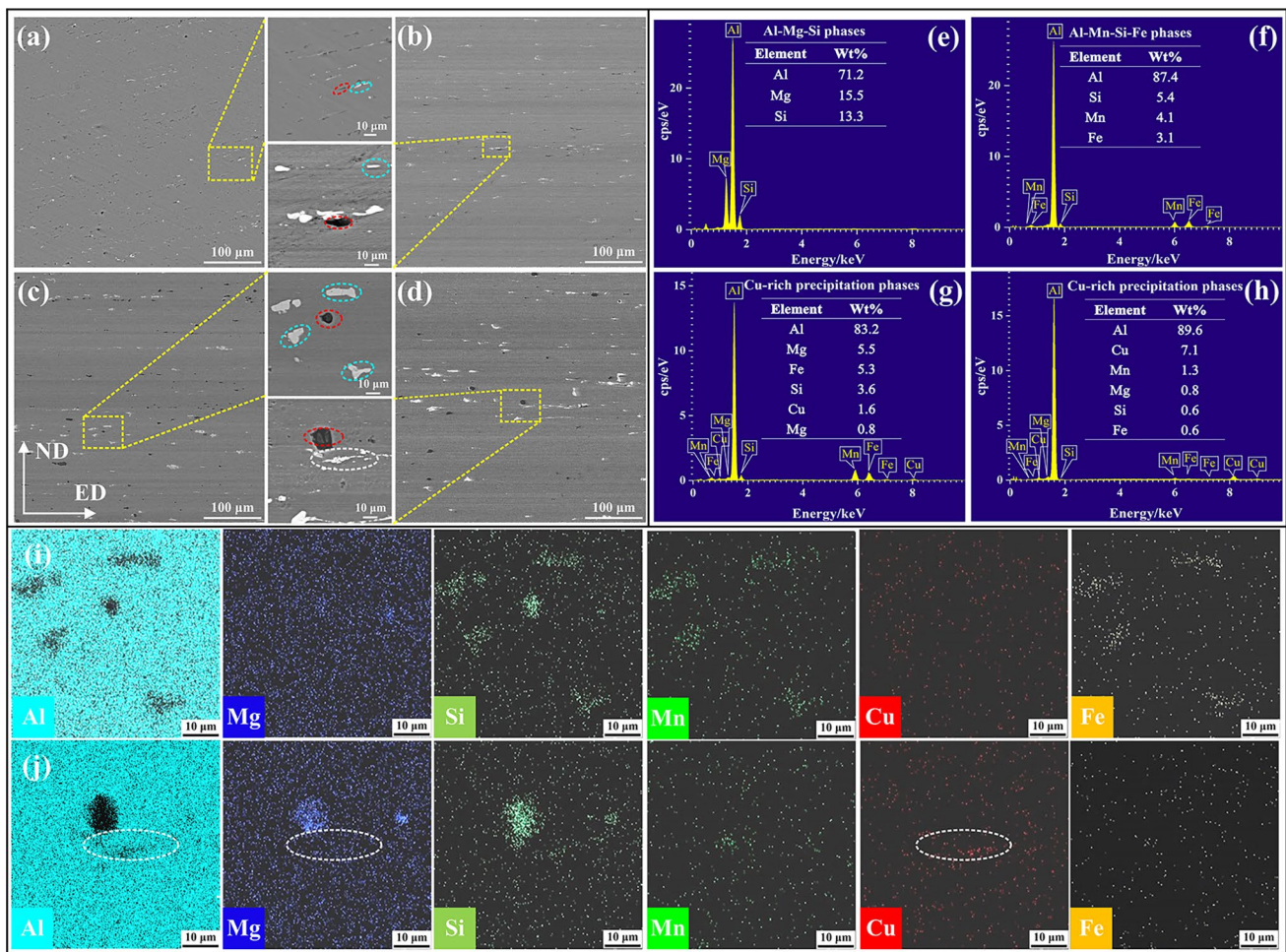

Fig. 6 SEM and EDS of four extruded alloys: **a** ES-0Cu; **b** ES-0.6Cu; **c** ES-1.3Cu; **d** ES-2.0Cu; **e–h** content of black and white precipitate phase elements; **i** and **j** EDS element scanning maps for ES-1.3Cu and ES-2.0Cu
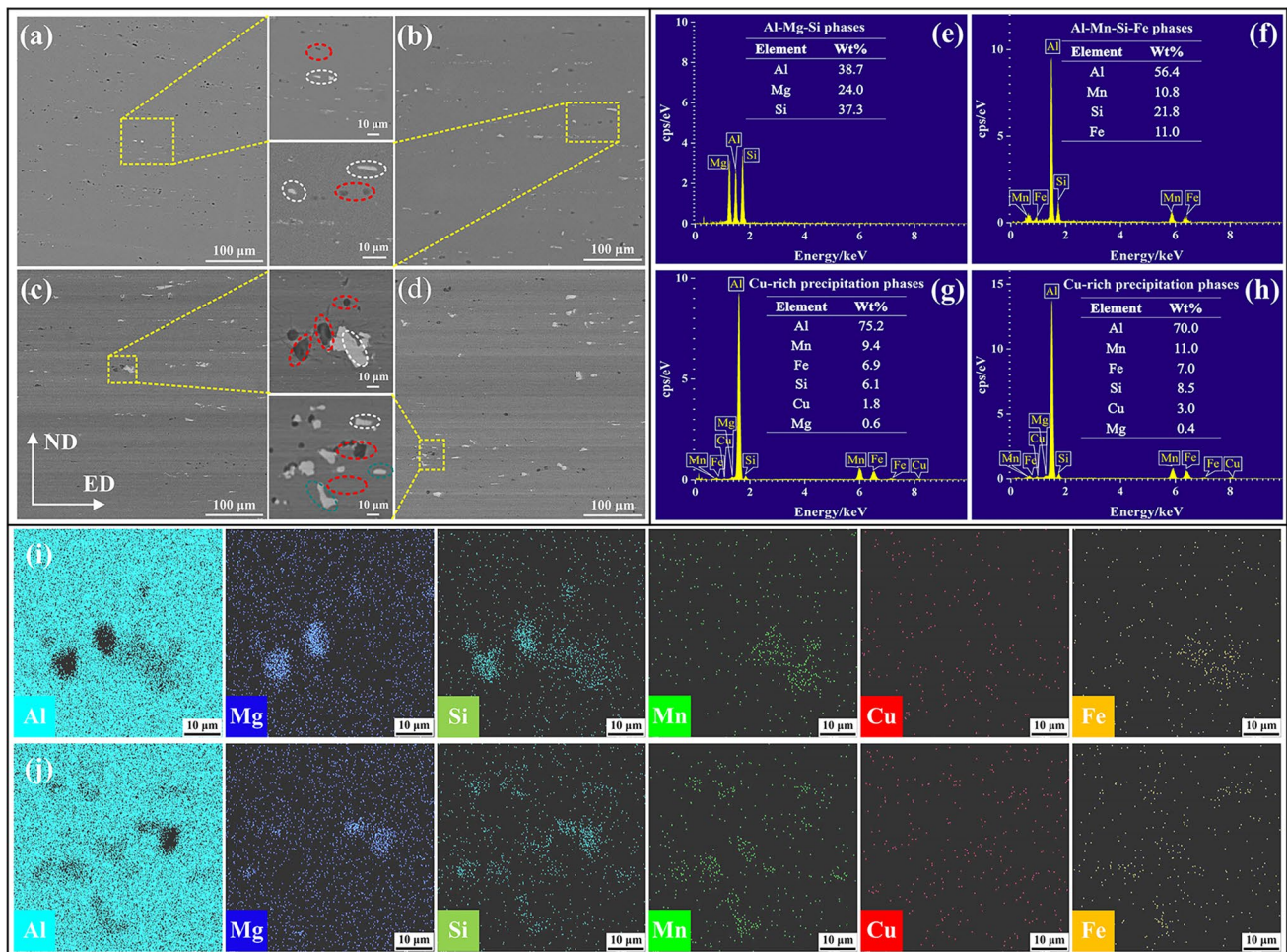
Fig. 7 SEM and EDS of four T6-treated alloys: **a** SA-0Cu; **b** SA-0.6Cu; **c** SA-1.3Cu; **d** SA-2.0Cu; **e–h** content of black and white precipitate phase elements; **i** and **j** EDS element scanning maps for SA-1.3Cu and SA-2.0Cu

in the microstructure of the extruded and T6-treated alloy were mainly rich Mg-Si-Mn-Fe phase. The distribution of Cu element was relatively uniform, and only a small amount of Cu element accumulated in SA-2.0Cu (white oval area in Fig. 6j). The segregation of Cu in the alloy was not obvious, which may be due to the high solid solubility of Cu in the Al matrix. Even if the precipitation of Cu occurred, the segregation was mainly carried out in the rich Mg-Si-Mn-Fe phase.

From Figs. 6i-j and 7i-j, it can be clearly seen that the black and white precipitated particles were composed of different elements, indicating the presence of distinct phases within these particles. Subsequently, EDS point scanning was conducted. In the case of ES-0Cu, the black precipitated phase was predominantly rich Mg-Si phase (Fig. 6e), while the white precipitated phase was mainly rich Al–Fe-Mn-Si phase (Fig. 6f). For the three Cu-containing alloys after extrusion treatment, the black precipitates remained mainly rich Mg-Si phases, while the white precipitates were mainly rich Al-Cu-Mn-Si-Fe

phases (Fig. 6g, h). To further determine the possible form of precipitation, XRD phase analysis was performed, as indicated in Fig. 8.

Based on the phase composition of each alloy in Fig. 8 and in combination with relevant literature [19, 20, 32], it can be speculated that the black rich Mg-Si phase in all extruded samples was Mg_2Si phase, and the white rich Al–Fe–Mn–Si phase was a mixed phase composed of Al_5FeSi, α-Al(FeMn)Si and AlCuMg. After T6 treatment, the black Mg_2Si phase was still observed in all T6-treated alloys. However, no Al_5FeSi was found in the XRD pattern, suggesting that the Al_5FeSi generated during extrusion may have transformed into α-Al(FeMn)Si [10]. For the three Cu-containing alloys after T6 treatment (combined with SEM and XRD results), the black rich Mg-Si phase should be still identified as the Mg_2Si phase, while the white rich Al-Cu-Mn-Si-Fe phase was a mixed phase (by α-Al(FeMn)Si and AlCuMg). A similar phenomenon was also reported in the study by Wu et al. [19].
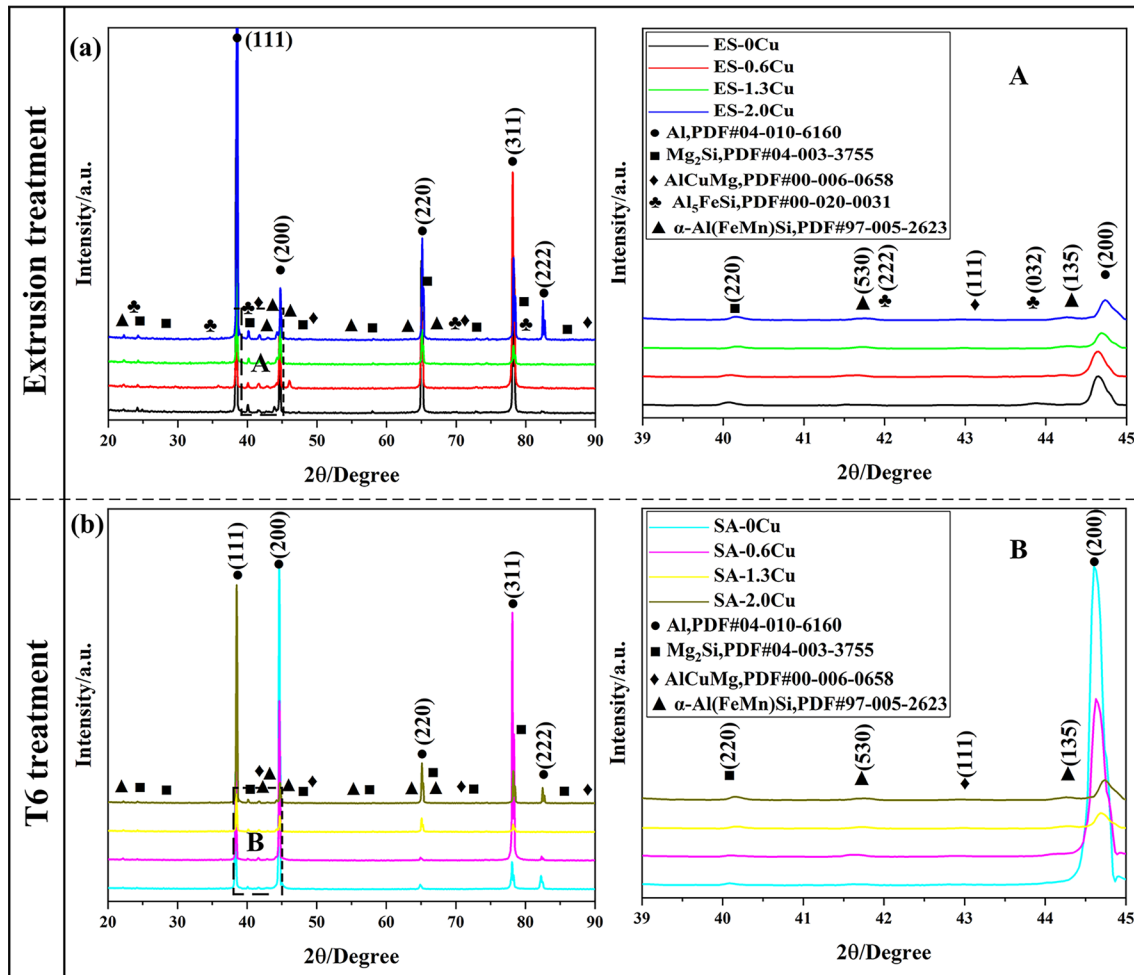
Fig. 8 XRD diagram of **a** extruded alloys and **b** T6-treated alloys

3.3 Grain Boundaries and Recrystallization

The grain boundary distribution characteristics can reflect the recrystallization degree of the alloy. The recrystallization degree, in turn, affects the grain size and dislocation distribution, which ultimately influence the mechanical properties. Therefore, analyzing the grain boundary characteristics of the four alloys and understanding their recrystallization situation can help elucidate the relationship between microstructure and properties [33]. Figure 9 gives the recrystallization situation of the extruded sheets. In the grain boundary diagram, high-angle grain boundaries (HAGBs: > 15°) and low-angle grain boundaries (LAGBs: 2°–15°) are represented by black and blue lines, respectively [27]. The microstructure of the four extruded alloys still contained a certain number of LAGBs. Among them, the ES-0Cu and ES-0.6Cu alloy sheets had LAGBs of about 30.1%, with corresponding sub-grain proportion of 37.6% and 48.2%, respectively. With the further addition of Cu, the percentage of sub-grain grains further increased to about 54.9%. However, there

was a tendency for the percentage of deformed grains to decrease, with values of 33.8% (ES-1.3Cu) and 22% (ES-2.0Cu), respectively. The statistical results indicated that the addition of Cu increased the percentage of substructures and recrystallized grains while decreasing the percentage of deformed grains. This suggested that the presence of Cu might promote the transition from deformed grains to subgrains and recrystallized grains. Go et al. [34] pointed out that the precipitated phase particles formed by the addition of other elements to alloys accumulate a large amount of strain energy around the precipitated phase during thermal deformation, which can act as nucleation point for recrystallized grains. The addition of Cu increased the number of precipitated phases, providing sites for the nucleation of the recrystallized grains. Although there is no extensive recrystallization during the extrusion process, the addition of Cu promotes the transformation of deformed grains to sub-grains and recrystallized grains.

Figure 10 displays the grain boundary characteristics, orientation angle distribution and grain morphology of the alloy
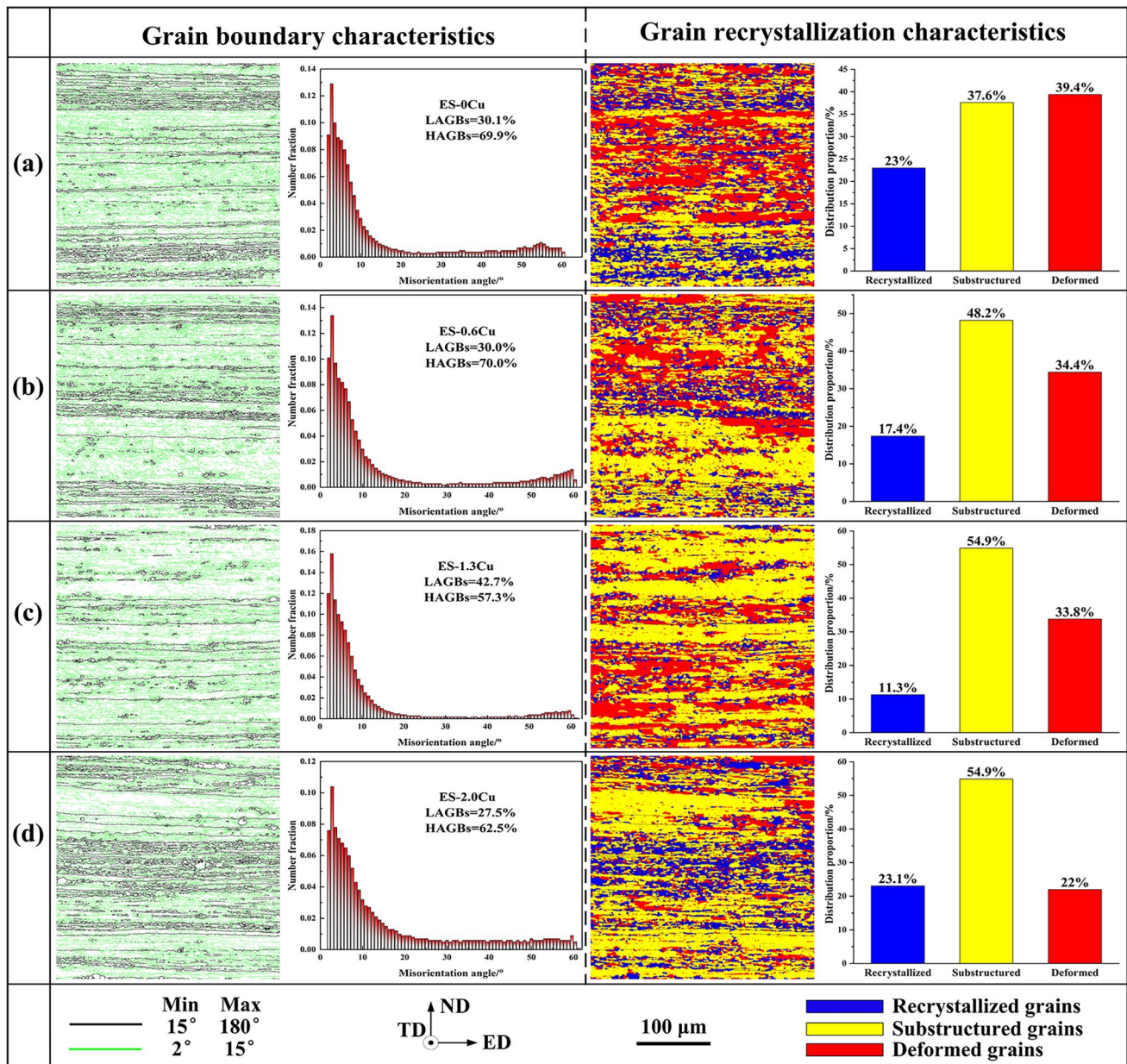
Fig. 9 Grain boundaries characteristics and recrystallization condition of four extruded alloys: **a** ES-0Cu; **b** ES-0.6Cu; **c** ES-1.3Cu; **d** ES-2.0Cu

after T6 treatment. The HAGBs of the four alloys accounted for about 97%, and the number of LAGBs was significantly lower compared to extruded sheets, and the percentage of deformed grains was 0%. The four extruded alloys generated a large number of substructures, which continuously absorbed residual dislocations in the microstructure at high temperatures. Adjacent substructures would also merge and finally transformed into HAGBs, leading to the difficulty of observing LAGBs in the microstructure after solution treatment. The annihilation of substructures and residual dislocations had a negative effect on the improvement of the yield strength of the alloy. However, the growth of grains and the

annihilation of dislocations and substructures within grains were beneficial for the metal to store more dislocations during deformation, thereby exhibiting good plasticity.

3.4 Hardness and Tensile Property

Figure 11 exhibits the hardness distribution of four alloys after extrusion and T6 treatment. As shown in Fig. 11a-d, the addition of Cu led to a continuous decrease in the area of the colored rhombus in the extruded sheets, indicating an increasing trend in alloy hardness. The average hardness values of four extruded alloys were 45.9 HV, 60.1 HV, 66.7
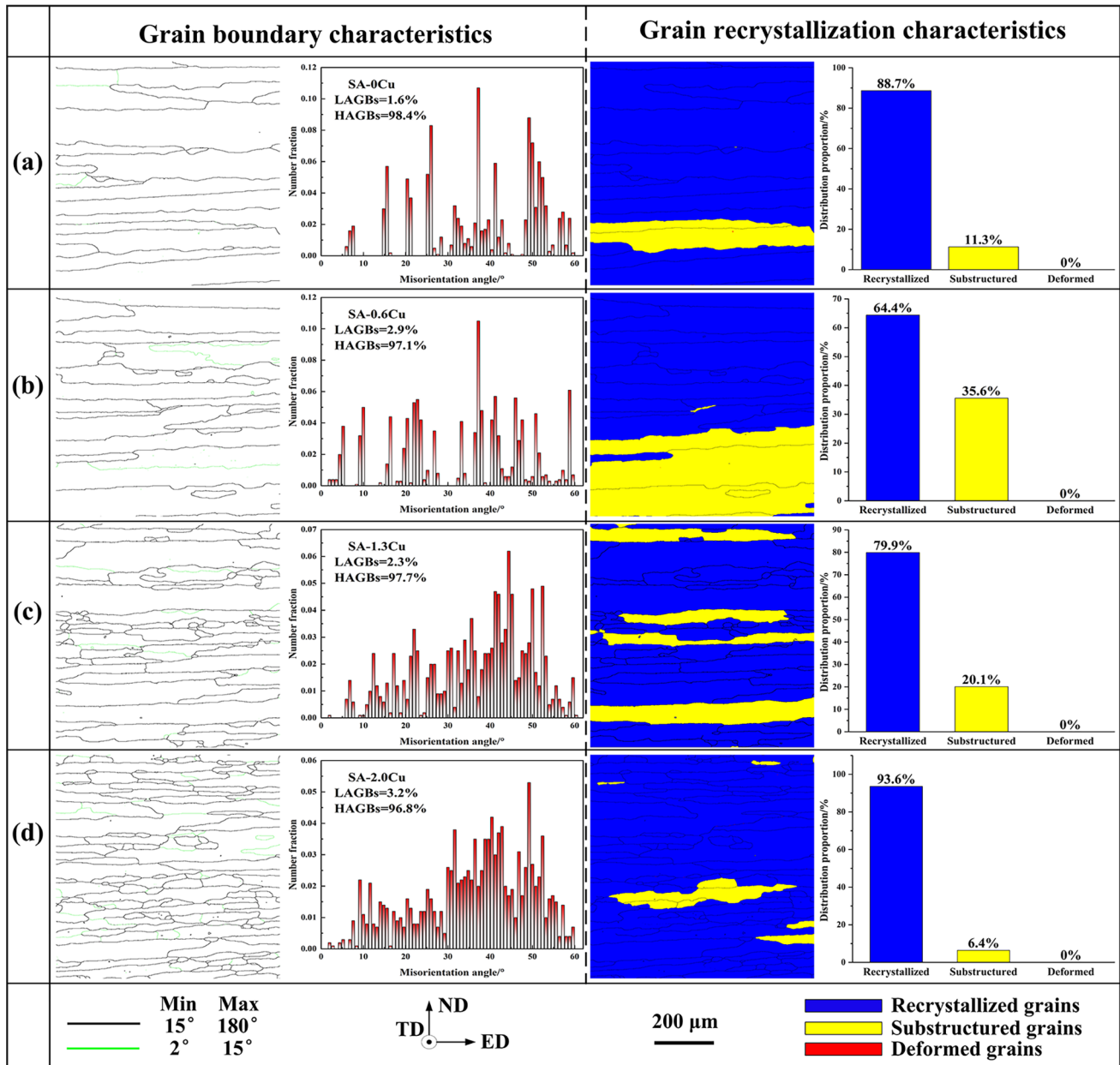
Fig. 10 Grain boundaries characteristics and recrystallization condition of four T6-treated alloys: **a** SA-0Cu; **b** SA-0.6Cu; **c** SA-1.3Cu; **d** SA-2.0Cu

HV and 87.1 HV, respectively. Notably, ES-2.0Cu exhibited a 90.1% increase in hardness compared to the ES-0Cu. Figure 11e–h displays the hardness result of the four alloys after T6 treatment. It can be seen that the addition of Cu was still effective in improving the hardness of the T6-treated alloys, and the hardness values of the four alloys were 116.8 HV, 132.9 HV, 138.2 HV and 150.9 HV, respectively. Compared with SA-0Cu, the hardness value of SA-2.0Cu increased by 34.1 HV.

Figure 12a and b exhibits the true stress–strain curves of alloys in different state. The yield strength (YS), ultimate tensile strength (UTS) and elongation (EL) for combinations of 6xxx alloys in current studies are summarized in Fig. 12c and d. As shown in Table 2, for the ES-0Cu alloy, the YS, UTS and EL of were 103.9 MPa, 158.9 MPa and 16.3%, respectively. After adding the Cu element, the YS and UTS of the extruded alloys indicated an increasing tendency. The YS values of 0.6 Cu, 1.3 Cu and 2.0 Cu in the ES were 130.5 MPa, 133.9 MPa and 200.2 MPa, respectively, while the UTS values were 204.5 MPa, 247.8 MPa and 301.5 MPa, respectively. It was worth noting that the elongation of the four alloys inclined firstly and then
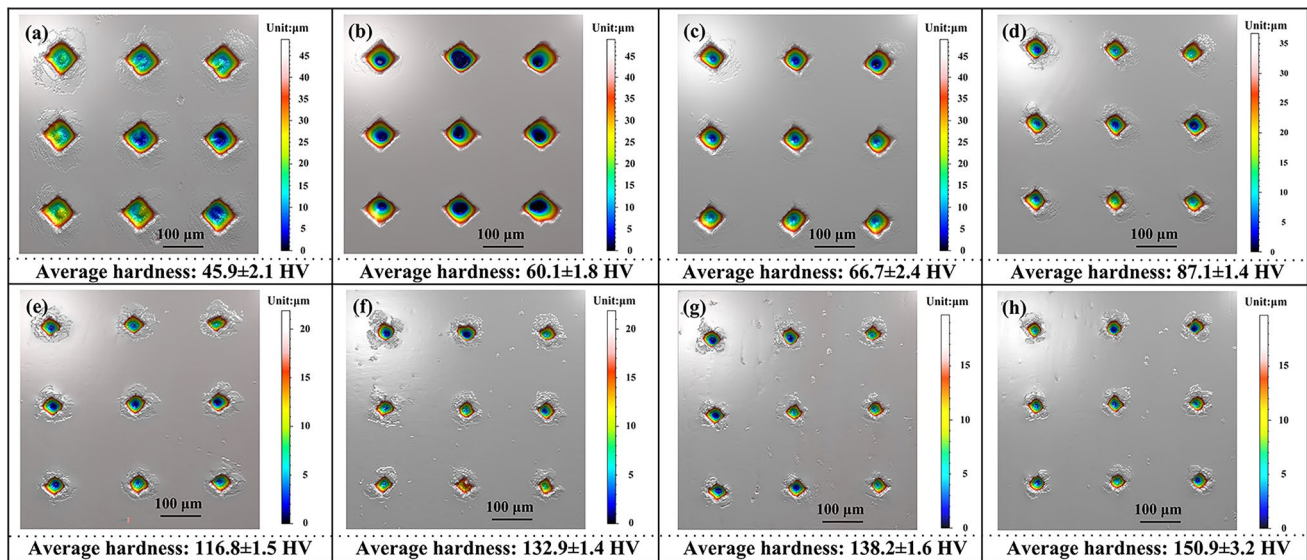
Fig. 11 Hardness diagrams of the extruded and T6-treated alloys: **a** ES-0Cu; **b** ES-0.6Cu; **c** ES-1.3Cu; **d** ES-2.0Cu; **e** SA-0Cu; **f** SA-0.6Cu; **g** SA-1.3Cu; **h** SA-2.0Cu

declined. The elongation of the four extruded alloys was 16.3%, 21.5%, 20.5% and 17.6%, respectively. In Fig. 12a, the four extruded alloys exhibited a zigzag yield phenomenon during stretching. This phenomenon resulted from the interaction between dislocations and solute atoms during the deformation process of materials [35].

The YS and UTS of the four T6-treated alloys were significantly improved compared to those of the extruded sheets, but EL was slightly reduced. Among them, the YS, UTS and EL of SA-0Cu were 275.9 MPa, 308.9 MPa and 12.0%, respectively, which were about 172.0 MPa and 150.0 MPa higher than those of ES-0Cu, with the elongation reduced by 4.3%. The YS values of SA-0.6Cu and SA-1.3Cu were 291.5 MPa and 312.2 MPa, respectively, with UTS values of 360.6 MPa and 381.6 MPa, and EL at break of 18.6% and 17.2%. Surprisingly, when the Cu content increased to 2.0%, the YS and UTS of the alloy increased to 342.9 MPa and 424.8 MPa, respectively, representing increases of 67.0 MPa and 115.9 MPa compared to SA-0Cu. Adding Cu to Al–Mg-Si-Mn alloys can significantly improve the strength of the alloy, whereas a small amount of Cu can promote its elongation, but excessive Cu can adversely affect its ductility. Finally, the mechanical properties of Al–Mg–Si–Mn sheets prepared by deformation treatment (extrusion or rolling) and heat treatment were compared with the 6xxx series Al alloy with different alloy compositions in existing studies, as shown in Fig. 12c and d. It can be observed that the four solution and aging alloys in this study had moderate YS and relatively excellent elongation, but the most obvious advantage was their strong UTS. In other words, this could provide theoretical

and technical references for the preparation of Al alloy profiles with complex shapes.

Figure 13 presents the fracture morphology of the tensile specimen, with the position of the enlarged morphology marked in the macroscopic view. The overall fracture of the four extruded alloys was relatively flat, with microscopic fracture morphology consisting of dimples and cleavage steps. Figure 13a is the fracture morphology of ES-0Cu. The A1 region in the middle possessed a certain number of dimples. In the peripheral A2 area, although dimples were still observed, their number decreased. For ES-0.6Cu, the number of dimples in the fracture (Fig. 13b) increased significantly (B1 area), and the size of the dimples became larger and deeper, suggesting increased plasticity. However, in ES-1.3Cu and ES-2.0Cu, the dimples in the fracture gradually became smaller and shallower, the area of the cleavage step became larger (Fig. 13c and d), and the fracture morphology tended to be flat, implying a gradual decrease in plasticity contribution. After T6-treated treatment, the fracture covered dimples, tear edges and cleavage steps, presenting ductile–brittle fracture characteristics. Previous literature [29] has reported that the tearing edge and the plane area are the manifestations of the plasticity reduction. In SA-0Cu (Fig. 13e), although few dimples were present in the E1 region, it was notable that flat areas and fine tear edges were observed in the fracture. The E2 region at the edge even showed some large plane regions, indicating reduced plasticity. In the F1 region of SA-0.6Cu (Fig. 13f), the number and size of dimples were obviously increased, yet some dissociation planes were also observed. The dissociation characteristics
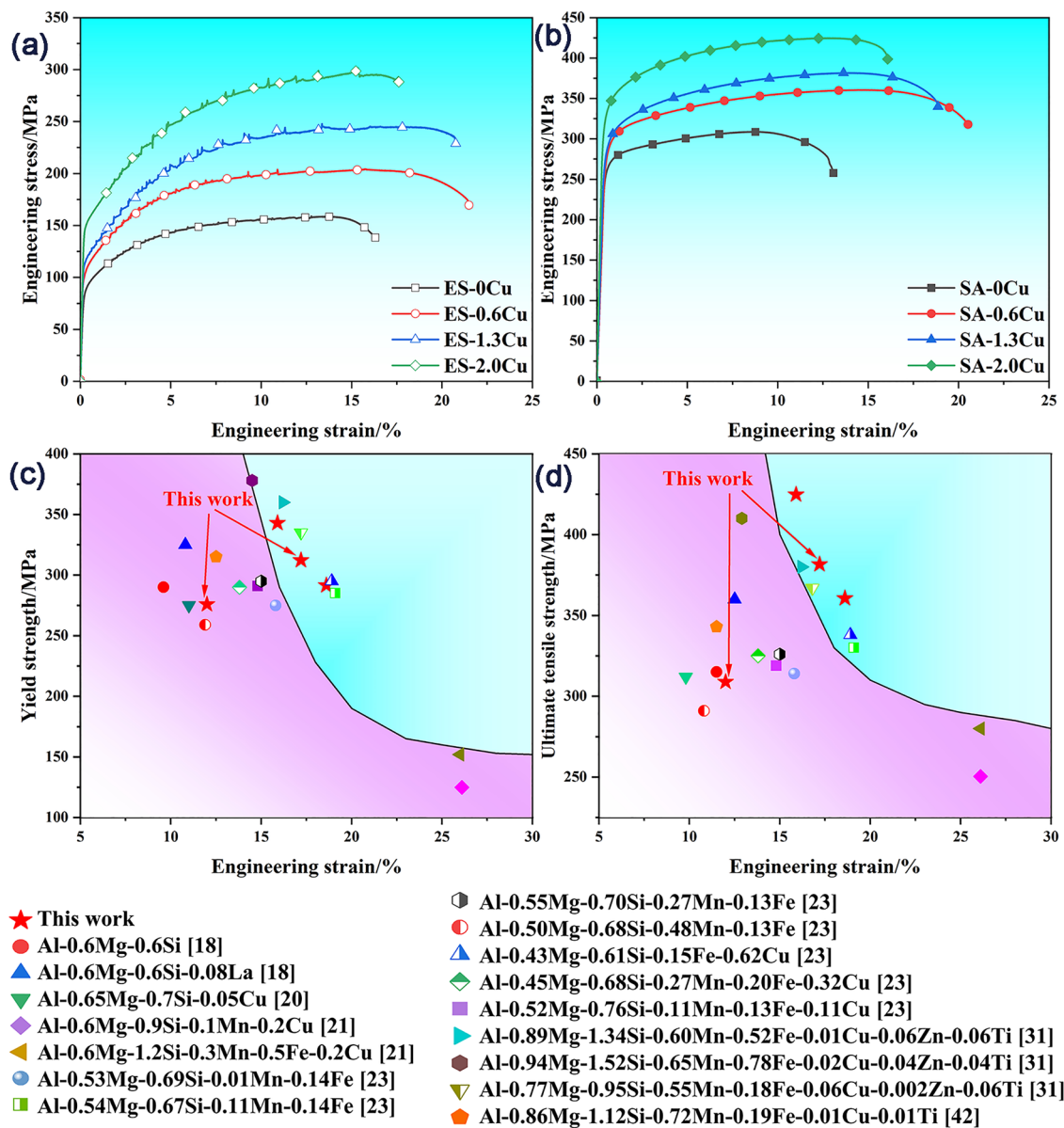
Fig. 12 Tensile engineering stress–strain curves of extruded samples: **a** tensile curves of the four extruded alloys; **b** tensile curve of the four T6-treated alloys; **c** YS and elongation combinations of 6xxx alloys; **d** UTS and elongation combinations of 6xxx alloys

Table 2 Mechanical properties of the four Al–Mg–Si–Mn alloys with different Cu contents at ES and SA states

Alloys	YS (MPa)		UTS (MPa)		El (%)	
	ES	SA	ES	SA	ES	SA
0Cu	103.9 ± 1.5	275.9 ± 1.9	158.9 ± 3.1	308.9 ± 2.5	16.3 ± 0.9	12.0 ± 1.6
0.6Cu	130.5 ± 2.6	291.5 ± 1.5	204.5 ± 2.8	360.6 ± 3.9	21.5 ± 0.8	18.6 ± 0.9
1.3Cu	133.9 ± 1.9	312.2 ± 2.8	247.8 ± 3.5	381.6 ± 4.9	20.5 ± 1.5	17.2 ± 2.3
2.0Cu	200.2 ± 1.1	342.9 ± 3.2	301.5 ± 2.4	424.8 ± 3.9	17.6 ± 2.3	15.9 ± 1.6

of the F2 region located at the edge were further intensified. With the addition of Cu, the tearing edge in the fracture became coarser, the plane area gradually increased, while the dimple became smaller and shallower, consistent with the elongation of the alloy. In summary, the fracture characteristics of the four alloy sheets under extrusion and T6 treatment conditions exhibited ductile–brittle fracture.
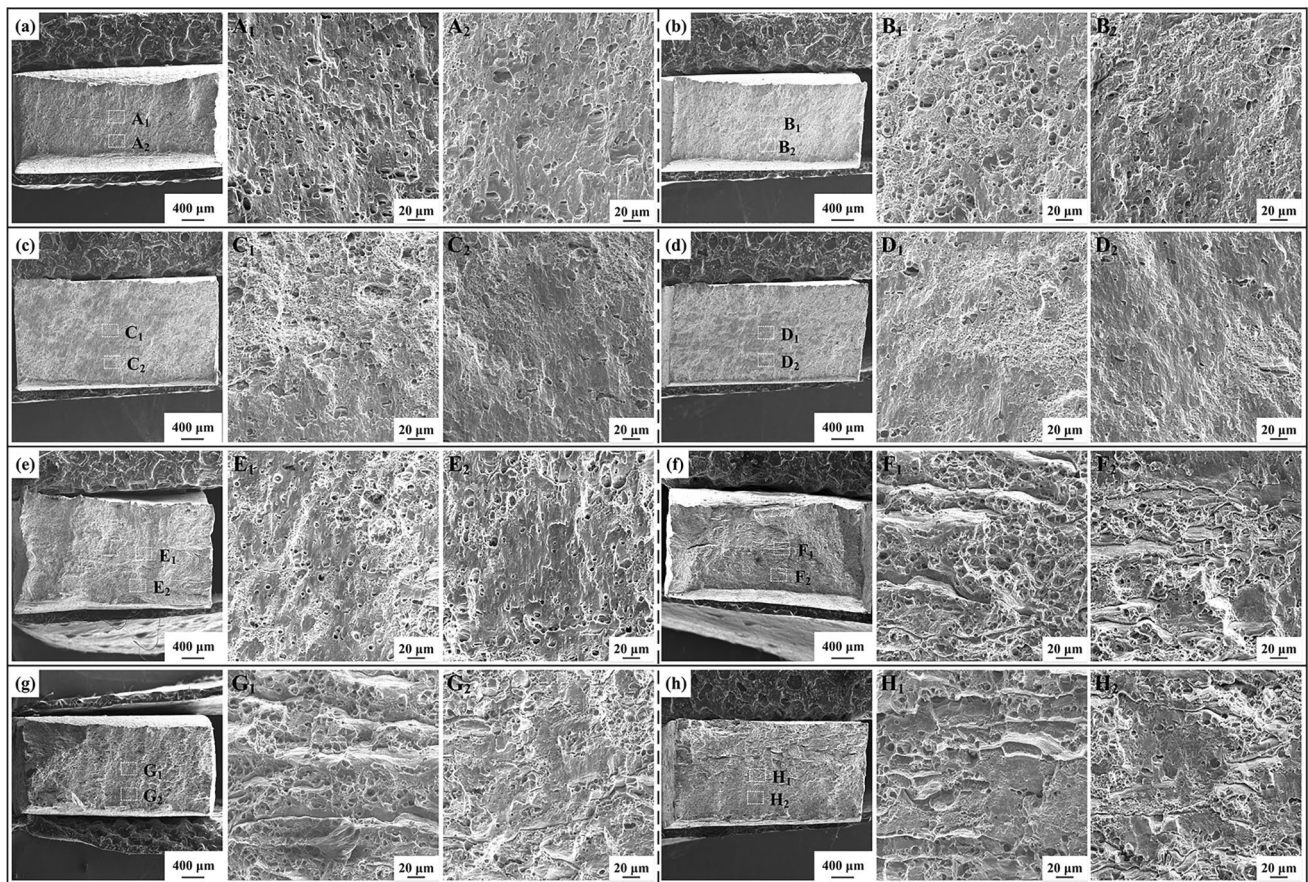
Fig. 13 Tensile fracture diagram in different states: **a** ES-0Cu; **b** SA-0Cu; **c** ES-0.6Cu; **d** SA-0.6Cu; **e** ES-1.3Cu; **f** SA-1.3Cu; **g** ES-2.0Cu; **h** SA-2.0Cu

4 Discussion

4.1 Micro-texture

As mentioned above, there is a certain difference in the distribution of PF and pole density for the four extruded alloys, which might be related to the type and quantity of texture in the alloys. To analyze the texture characteristics of the four extruded sheets, orientation distribution functions (ODFs) were plotted based on EBSD data. Figure 14 gives the ODF sections of four alloys at $\varphi2 = 45°$, 65° and 90°, and the ODF distribution diagram of the theoretical texture at $\varphi2 = 45°$ (as presented in the last line of Fig. 14). The extruded sheets textures of the four alloys mainly consisted of A*{111} < 112 >, Copper{112} < 111 > and P{001} < 566 > textures. In particular, the intensity of P-type texture was the most prominent in ES-0Cu. In ES-0.6Cu, the intensity of A*, Copper and P textures was enhanced, and each texture aligned closely with the pole position of the theoretical texture. As the Cu content increased further, the textures intensity of the alloys exhibited an increasing tendency, but the texture

types remained relatively unchanged and still contained A*, Copper and P textures.

For the four T6-treated alloys, significant changes in the orientation density position were observed after heat treatment. The texture types of the alloy mainly evolved into Cube {001} < 100 >, A {111} < 110 > and Goss{110} < 001 > textures, whereas the A*, Copper and P textures obviously weakened compared to the standard spectra. It can be clearly seen that the Cube texture was distributed on the four vertices of the square on the $\varphi2 = 90°$ section of SA-0Cu, and a small amount of A texture of {111}-fiber also appeared. The texture type inSA-0.6Cu alloy did not change much compared with SA-0Cu, but the corresponding texture intensity was reduced. Interestingly, new isodensity lines appeared in the ODF plots of SA-1.3Cu and SA-2.0Cu. Previous research by Hua et al. [36] suggested that when the annealing temperature is higher than 350 °C, Goss texture would form in the alloy. The proportion of Goss texture increases with the extension of the holding time. In the ODF diagram, the Euler angles and Miller indices of the Goss texture are (90°, 90°, 45°), (0°, 45°, 90°) and [110] < 001 >, respectively. The distribution positions of the above new isodensity line are
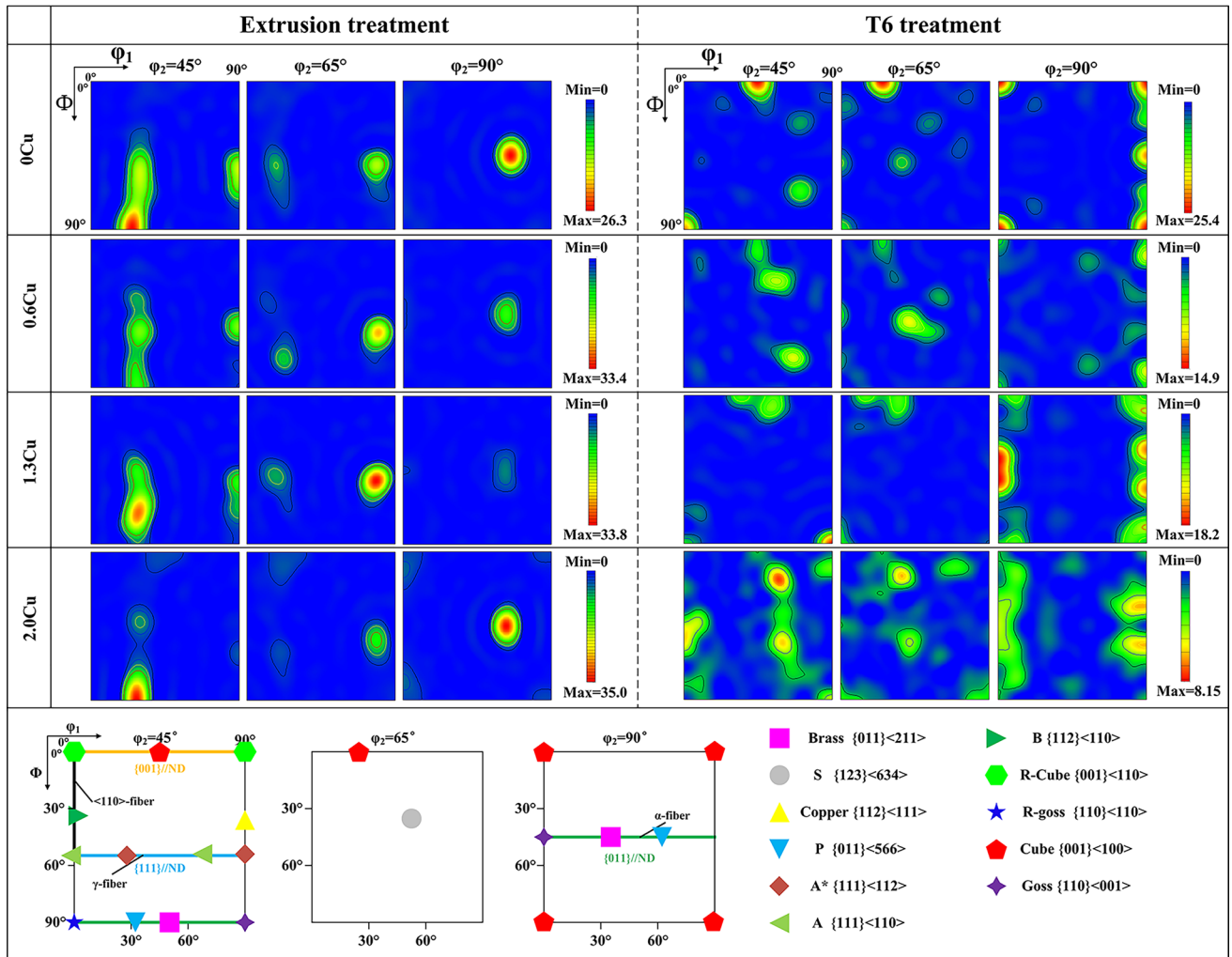
Fig. 14 Key to the position of the main ideal direction on φ2 = 45° section in ODF diagram

similar to the ideal Euler angles of Goss texture. Therefore, it can be considered that the Cu-containing alloys form a Goss texture after heat treatment.

In Fig. 14, texture components with higher intensity are easily observed, while some textures with weaker intensity in the alloy are difficult to be distinguished. To display the texture type of the alloy more intuitively and quantify it, the EBSD map was used to display the distribution of the texture in the microstructure (Fig. 15). The proportion of various textures was also counted, as seen in Fig. 16. The proportions of P and A* in the four extruded sheets varied significantly depending on the alloys, while Copper texture exhibited small variation and the proportions of the other types of textures were more limited. Besides, the microstructure not only covered some grains with theoretical texture characteristics, but also presented some randomly oriented layered grains. Specifically, the statistical result in Fig. 16 indicated that the proportion of P texture in ES-0Cu was

about 36.1%, and then with the addition of Cu, the proportion of P texture first decreased and then increased, but the proportion of P texture in the four alloys exceeded 20%. The proportion of A* texture in ES-0Cu was about 30.6%, and its value decreased first and then increased with the addition of Cu. The proportion of other theoretical texture components did not exceed 5%. The random texture in the extruded alloys inclined firstly and then declined with the increase of Cu. Liu et al. [37] also found that the texture type and proportion of the deformed alloy also varied greatly with the alloy composition and concluded that the difference in chemical composition in the alloys was the inducement of texture difference in the microstructure. It can be concluded that in this work, the changes in the texture types and contents of the four alloys are related to the addition of Cu.

Overall, after T6 treatment, the proportions of Cube, A and Goss textures in the microstructure increase significantly, while the proportions of A* and P textures are only
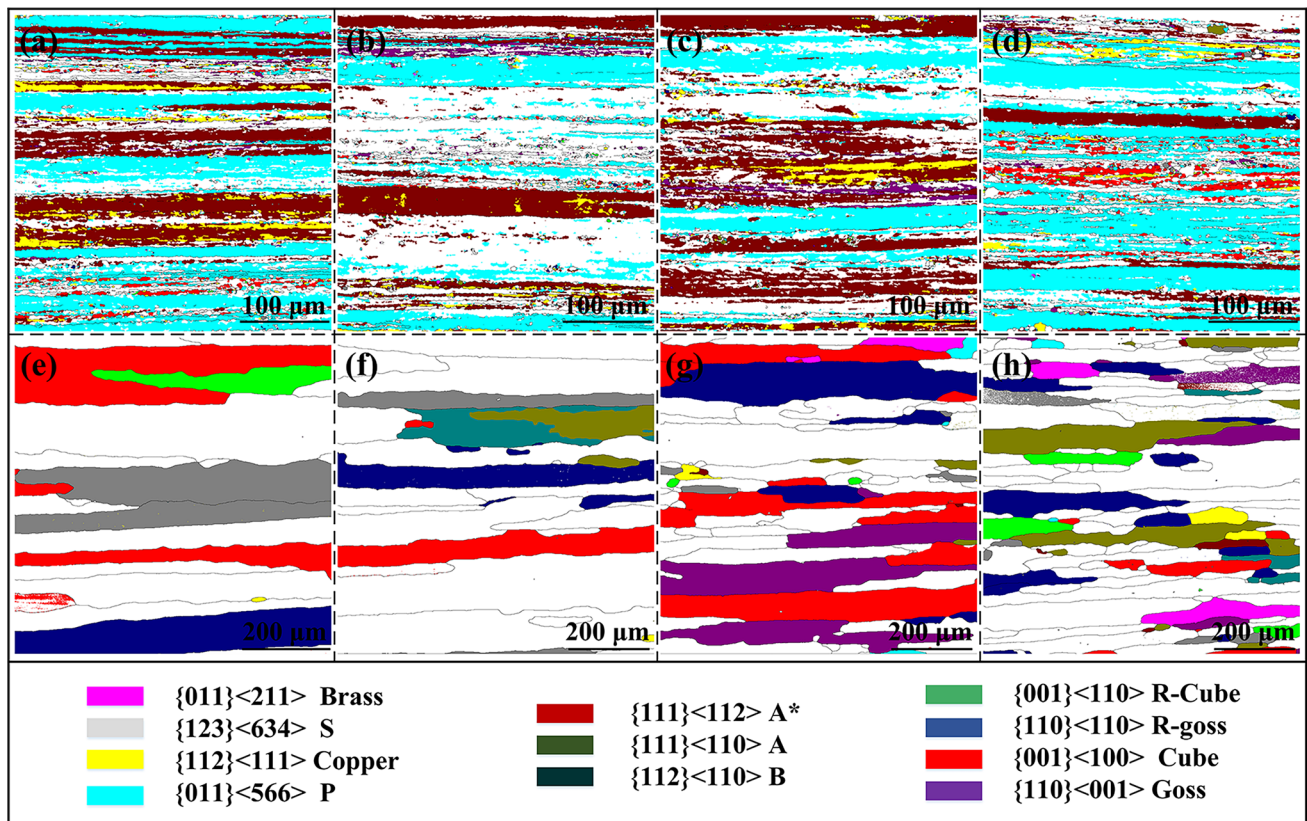
Legend:
- {011}<211> Brass (magenta)
- {123}<634> S (grey)
- {112}<111> Copper (yellow)
- {011}<566> P (cyan)
- {111}<112> A* (dark red)
- {111}<110> A (dark olive green)
- {112}<110> B (dark teal green)
- {001}<110> R-Cube (green)
- {110}<110> R-goss (blue)
- {001}<100> Cube (red)
- {110}<001> Goss (purple)

Fig. 15 Diagram of texture evolution: **a** ES-0Cu; **b** SA-0Cu; **c** ES-0.6Cu; **d** SA-0.6Cu; **e** ES-1.3Cu; **f** SA-1.3Cu; **g** ES-2.0Cu; **h** SA-2.0Cu

below 1%. In addition, the proportions of S, Copper, R-Cube and R-Goss textures gradually decrease with the increase of Cu. With the addition of Cu, the proportion of random texture in the alloy (> 32.0%) is generally higher than that of the alloy without Cu (25.0%). The proportion of the extruded alloy is different from that after T6 treatment due to lattice rotation changes in the texture type during the high temperature of solution process [36].

4.2 Mechanical Properties

The tensile stress–strain curves in Fig. 12 demonstrate that after the addition of Cu, the mechanical properties of the extruded alloys are significantly improved, and the strength of the alloys is further improved with the increase of Cu content. Generally, the factors that affect the mechanical properties of Al alloys mainly include grain size, precipitated phase, residual dislocations, etc. However, the grain sizes of the four extruded alloys in this study are found to be similar, ranging from 4.57 μm to 4.97 μm, and the differences in grain refinement with the addition of Cu are extremely limited. Therefore, the strength changes due to grain size can be ignored. Chen et al. [34] pointed out that the kernel average misorientation (KAM) maps could reflect the concentration of dislocations and strains in the microstructure, and the larger the KAM value, the greater the residual degree of dislocations and strains. High dislocations and strain residues can increase the strength of the alloy, but reduce the plasticity of the alloy. Figure 17 illustrates the distribution of the KAM maps for the four extruded alloys with averaged KAM values. The result demonstrated that the KAM values of the four extruded alloys were relatively close, indicating that the dislocation strengthening effect of the extruded alloy is relatively limited. Therefore, the reason why the alloys properties are improved after adding Cu should be related to other factors. In addition to being partially solidified in the matrix, Cu was also precipitated during the extrusion process, resulting in precipitation strengthening. The results of SEM and XRD displayed that no Cu-containing phase was observed in the precipitated phases of the ES-0.6Cu alloy, implying that Cu may mainly remain in the Al matrix in the form of solution. The maximum solubility of Cu in solid phase aluminum is 5.65 wt%, and the composition of the eutectic point is 32.7 wt% Cu [38]. Due to the large difference in the volume of Cu atoms and Al atoms, lattice distortion is caused, and an elastic stress field is generated. This stress field interacts with dislocations and hinders the movement of dislocations. Thus, it can be considered that
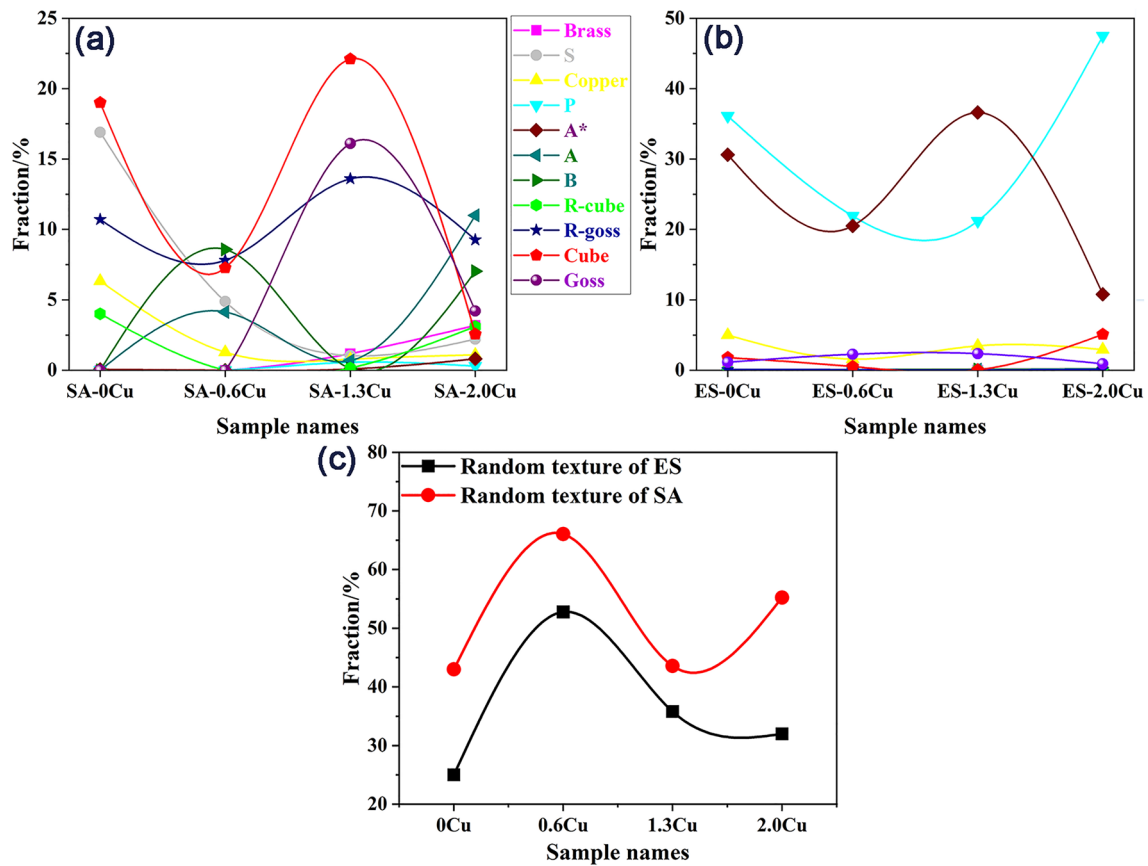
Fig. 16 Proportion diagram of different textures: **a** different texture proportions of four extruded alloys; **b** different texture proportions of four T6-treated alloys; **c** random texture of alloys in two different states

the addition of 0.6 wt% Cu to the matrix has a better solid solution strengthening effect. Jin et al. [39] added less than 0.6 wt% Cu to the Al–Mg–Si alloy and found that the addition of Cu could improve the strength and plasticity. As the Cu continued to increase, Cu-containing phases (such as AlCuMg) also appeared in the alloy, which enabled the alloy to have both solid solution strengthening and precipitation strengthening effects, further enhancing its strength. Yoshida et al. [40] pointed out that the formability of the alloy was greatly affected by the work hardening rate. The higher the work hardening rate of the material, the better the plasticity. It is believed that Cube and Random textures provide higher work hardening rate to aluminum alloys. In other words, the higher the proportion of Cube and Random textures in the alloy, the better the plasticity of the alloy. Figure 16c indicates that the proportions of random texture in the four extruded alloys were 25.0%, 52.7%, 35.8% and 32.0%, respectively. This result was consistent with the elongation exhibited by the alloys (inclined firstly and then declined in plasticity). Therefore, it can be seen that the addition of Cu not only increases the proportion of random texture in the microstructure but also improves the plasticity of the alloy.

The strength of T6-treated sheets has been reported to be significantly improved compared with the extruded sheets, as observed in many Al alloys [12, 19]. The IPF diagram reveals that the grain size of the sheets coarsens significantly after solution treatment, which is not conducive to the improvement of its strength. However, this can reduce the binding of dislocation between sheets during stretching and the possibility of early stress concentration. After the grain growth, there is more space to accommodate dislocations, leading to ultimately exhibiting good plasticity. Furthermore, studies have demonstrated that texture also affects the plasticity of Al alloys. Hua et al. [36] concluded that the Schmidt factor (SF) of the slip system under the influence of texture had a strong effect on the room temperature plasticity of Al alloys. When the tensile load is in the extrusion direction at room temperature, the recrystallized textures (Cube and Goss) have a higher SF of 0.41 along the {111} slip system, while the Copper and P textures have an SF value of only 0.27. The high SF value makes dislocations more likely to move along the slip bands, resulting in more susceptible plastic deformation in the presence of an external force. It should be emphasized that the proportion of the
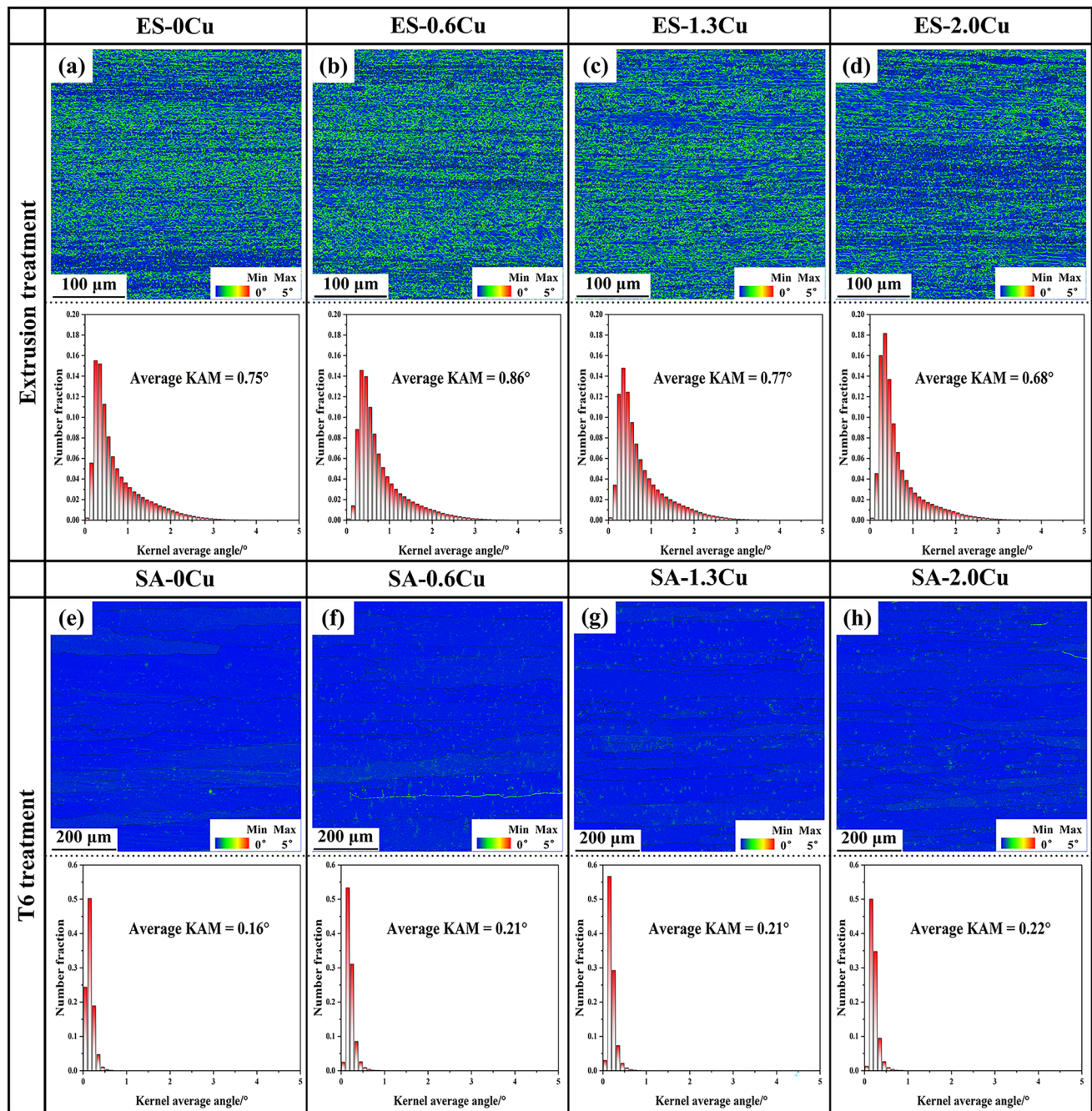
Fig. 17 Maps of KAM: **a** ES-0Cu; **b** SA-0Cu; **c** ES-0.6Cu; **d** SA-0.6Cu; **e** ES-1.3Cu; **f** SA-1.3Cu; **g** ES-2.0Cu; **h** SA-2.0Cu

sum of A *, Copper and P textures in the extruded alloy is higher than the proportion of the sum of Cube, A and Goss textures in the T6-treated alloy in this article. The above factors may be the reason why the alloy the T6-treated alloys exhibit close plasticity to the extruded alloys. Compared with extruded alloys, T6-treated alloys show a relatively weaker hardening ability. This may be due to the presence of more dislocations remaining in the extruded microstructure, which significantly intersect and entangle with newly

formed dislocations, limiting their movement and exhibiting stronger hardening ability.

Moreover, after T6 treatment, the amount of the second phases in the microstructure is bound to increase further, contributing to the precipitation strengthening effect and high strength of the T6-treated sheets. However, the SEM results reveal a decreasing trend in the number of second phases in the T6-treated sheet, contrary to expectations. This may be due to the limited observation ability of SEM,

and finer phases in the microstructure are not observed. Due to the better performance of SA-1.3Cu alloy in strength and plasticity among the four alloys, TEM observations were conducted on SA-1.3Cu alloy, as shown in Fig. 18. In Fig. 18a and d, a large number of ellipsoidal and rod-shaped precipitates with a size of about 500 nm could be observed. Two different points (P1 and P2) in Fig. 18b were scanned, revealing that they were rich Al-Mn-Fe-Si phases. Figure 18e shows the EDS mapping results in region A of SA-1.3Cu, indicating that some Mg atoms and Cu atoms in the alloy were solid-dissolved in the matrix. According to the research of Liu et al. [13, 22], adding a small amount of Cu to Al–Mg–Si alloy produces a dispersoid of α-Al(FeMn) Si in the alloy. This implies that some elements of the alloy are solid-dissolved in the matrix after T6 treatment to play the role of solid solution strengthening, while the remaining alloy elements precipitate in the form of second phase or dispersoid to achieve the effect of precipitation strengthening.

Figure 12 shows that the YS of the T6-treated alloy increases with the addition of Cu. The effects of fine grain strengthening (σ_{gs}), solid solution strengthening (σ_{ss}) and dislocation strengthening (σ_d) on the YS of Al–Mg–Si–Mn(–Cu) alloys are investigated with respect to the changes in the YS of the T6-treated alloys. Fine grain strengthening (σ_{gs}) represents the effect of grain size on YS, and the following Hall–Petch formula can be used [41]:

$$\sigma_{gs} = \sigma_0 + kd^{-\frac{1}{2}} \tag{1}$$

where σ_0 represents the friction stress of pure aluminum (~ 10 MPa [19, 42]), k [43] represents a common constant in aluminum which is 0.14 MPa m^{1}, and d represents the average grain diameter. In Fig. 4, the grain diameters of the four alloys are measured as 146.02 μm, 112.38 μm, 59.80 μm and 55.60 μm, respectively. The contribution of fine grain strengthening (σ_{gs}) to the strength is 21.29 MPa, 23.21 MPa, 28.10 MPa and 28.78 MPa.

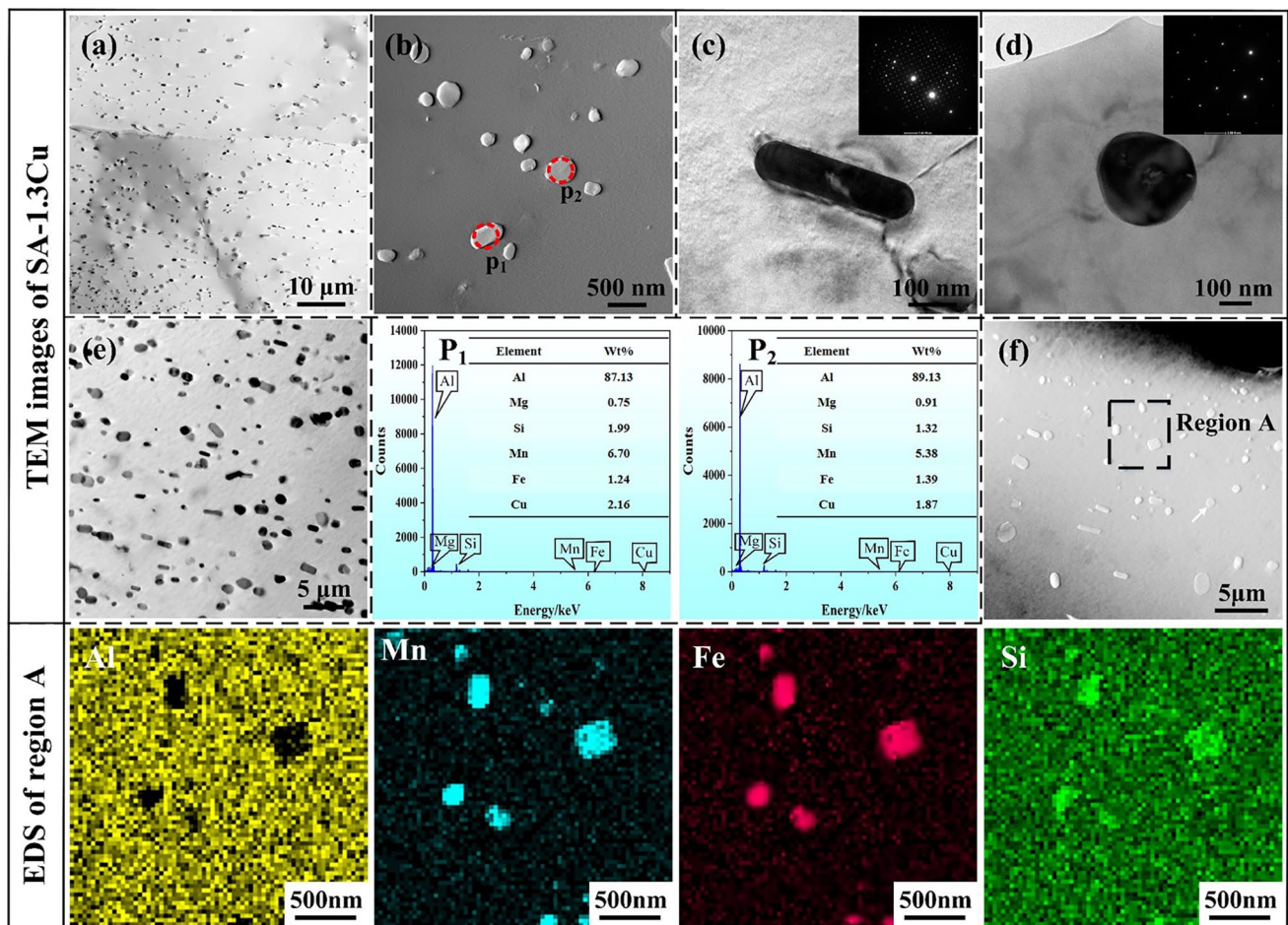For dislocation strengthening (σ_d) in Al alloys, the following Taylor equation [44] can be used to calculate:

Fig. 18 **a**, **b**, **e** and **f** TEM images of SA-1.3Cu. EDS analysis was conducted on the TEM images of the two points in **b** and the region A in **f**; **c** and **d** are high-resolution images of different shapes in the alloy

$$\sigma_d = M\alpha G b \rho^{1/2} \tag{2}$$

where M is the Taylor factor (i.e., 3.06), α is the content (fcc metal is 0.2), G is the shear modulus (i.e., aluminum alloy is 27 GPa) [27, 42], b is the Burgers vector (0.286 in aluminum alloy nm) [45], ρ is the dislocation density. Figure 17 gives the distribution of KAM maps of the four alloys. The KAM values of the four T6-treated alloys are relatively close, fluctuating around 0.2, and the fluctuation value is lower than 0.1. This indicates that dislocation strengthening of the T6-treated alloys has little effect. Consequently, the dislocation strengthening of the alloy is negligible [22].

The mechanical properties of solute atoms to YS are proportional to the concentration of solute atoms [19]. Assuming that the effects of each element on the mechanical properties can be superimposed, their overall influence can be calculated using the following formula [45]:

$$\sigma_{ss} = \sum_i k_i C_i^{\frac{2}{3}} \tag{3}$$

According to the research of Myhret et al. [46], the proportional coefficients k_i of Mg, Si and Cu are 29.0 MPa/wt./%$^{2/3}$, 66.3 MPa/wt./%$^{2/3}$, 46.4 MPa/wt./%$^{2/3}$, respectively; C_i represents the mass fraction of element i involved in solid solution strengthening. To reduce the influence of variables controlling the experimental process, it is assumed that all Mg atoms are dissolved in the Al matrix after solid solution treatment, and 60% of the solute atoms formed precipitated phases after aging. During the aging process, Cu atoms will form precipitated phases, resulting in a decrease in the Cu content in the matrix. Combined with existing studies [47], it is assumed that Cu contributes to 20% of the solid solution strengthening in the T6-treated treatment. The solubility of Si atoms consists of three parts. The first part is i a small amount of excessive Si presented in the solution alloy, but in this paper there are an excessive of Mg elements and fewer Si atoms remained. For simplicity, this part of Si will not be considered in the calculations. The second part is that some Si atoms are involved in the formation of Mg$_2$Si (Mg/Si = 1.73) [32] during the peak aging, rather than precipitation. The third part forms a Si-containing precipitated phase, consisting of α-Al(FeMn)Si. Assuming that the concentration of the phase bound to Fe is 0.059 [19] and that the precipitated phase contained both Mg to Si in mass ratio (~0.86), $C_{Si}^{depleted}$ can be calculated by formula (7):

$$C_{Si}^{depleted} = 0.86 \times 0.6 C_{Mg}^{total} \tag{4}$$

Therefore, the concentrations of Mg, Cu and Si can be calculated:

$$C_{Mg} = 0.4 C_{Mg}^{total} \tag{5}$$

$$C_{Cu} = 0.2 C_{Cu}^{total} \tag{6}$$

$$C_{Si} = C_{Si}^{total} - C_{Si}^{Fe-bearing phase} - C_{Si}^{depleted} \tag{7}$$

Using the above formulas and then brought into formula (3), the C_{Mg}, C_{Cu} and C_{Si} of the four alloys can be calculated, respectively. The solid solution strengths of the four alloys are then calculated to be 24.63 MPa, 33.12 MPa, 36.96 MPa and 42.12 MPa, respectively. Without considering the role of dislocation strengthening (σ_d), the values of fine grain strengthening (σ_{gs}) and solid solution strengthening (σ_{ss}) are calculated according to the formula. The results imply that the yield strength of the alloys is affected by these two main strengthening mechanisms and increases gradually with the addition of Cu.

Although the grain size of the extruded sheets is much finer, there are a large number of residual dislocations and strains within it (Fig. 17), causing dislocations entanglement and stress concentration, which lead to premature fracture and poor performance. For T6-treated alloys, the residual dislocations are consumed in large quantities, which reduces the entanglement between residual dislocations. And the larger grain space also provides more space to accommodate the dislocations generated during the deformation process. Additionally, the aging treatment promotes the formation of a larger number of precipitated phases with finer sizes, resulting in a better aging-strengthening effect. Consequently, the T6-treated sheets present a higher strength while maintaining good plasticity.

5 Conclusions

In this paper, the effect of extrusion and T6 treatment on Al–Mg–Si–Mn alloys with different addition of Cu elements was systematically investigated. The relationship between microstructure and mechanical properties of the different alloy sheets was discussed in detail. The following main conclusions were as follows:

1. After extrusion, the addition of Cu content resulted in a typically elongated grain microstructure, with minimal changes in grain size. Furthermore, the extruded alloys presented deformed textures such as A*, Copper and P textures, with random textures firstly increasing and then decreasing with increasing Cu content. After T6 treatment, the grain size of the four alloys significantly coarsened compared to the extruded state, but gradually decreased with the increase of Cu content. The recrystallized textures (Cube, A and Goss textures) dominated the texture components of the T6-treated alloys.

2. Due to a large amount of residual dislocations and precipitated phases in the extruded alloys, the hardness and strength showed a gradual increase trend with increasing Cu content. The corresponding tensile ductility first increased and then decreased, which was related to the evolution of random texture components.

3. Similar to the extruded state, the strength and hardness of the T6-treated four alloys showed an incremental trend with increasing of Cu content, especially when the Cu content was 2.0 wt%, the YS and UTS of Al alloy increased to 342.9 MPa and 424.8 MPa, respectively, while remaining an EL of 15.9%, which achieved a good balance of strength and ductility. The enhanced strength and elongation were primarily attributed to the abundance of fine precipitated phases and low dislocation density induced by T6 treatment.

Declarations

Conflict of interest The authors state that there are no conflicts of interest to disclose.

References

[1] J. Hirsch, Trans. Nonferrous Met. Soc. China **24**, 1995 (2014)

[2] O.F. Hosseinabadi, M.R. Khedmati, Ocean Eng. **232**, 109153 (2021)

[3] M. Aamir, K. Giasin, M. Tolouei-Rad, A. Vafadar, J. Mater. Res. Technol. **9**, 12484 (2020)

[4] X.H. Fan, D. Tang, W.L. Fang, D.Y. Li, Y.H. Peng, Mater. Charact. **118**, 468 (2016)

[5] C. Zhang, C. Wang, Q. Zhang, G. Zhao, L. Chen, J. Mater. Process. Technol. **270**, 323 (2019)

[6] J.J. Sidor, R.H. Petrov, L.A.I. Kestens, Mater. Charact. **62**, 228 (2011)

[7] W. Chrominski, M. Lewandowska, Acta Mater. **103**, 547 (2016)

[8] J. Buha, R.N. Lumley, A.G. Crosky, K. Hono, Acta Mater. **55**, 3015 (2007)

[9] T. Abid, A. Boubertakh, S. Hamamda, J. Alloys Compd. **490**, 166 (2010)

[10] N.C.W. Kuijpers, F.J. Vermolen, C. Vuik, P.T.G. Koenis, K.E. Nilsen, S.V.D. Zwaag, Mater. Sci. Eng. A **394**, 9 (2005)

[11] X. Xu, Z. Yang, Y. Ye, G. Wang, X. He, Mater. Charact. **119**, 114 (2016)

[12] L. Ding, Z. Jia, Z. Zhang, R.E. Sanders, Q. Liu, G. Yang, Mater. Sci. Eng. A **627**, 119 (2015)

[13] J. Rakhmonov, K. Liu, P. Rometsch, N. Parson, X.G. Chen, J. Alloys Compd. **861**, 157937 (2021)

[14] X.P. Ding, H. Cui, J.X. Zhang, H.X. Li, M.X. Guo, Z. Lin, L.Z. Zhuang, J.S. Zhang, Mater. Des. **65**, 1229 (2015)

[15] Y. Weng, L. Ding, Z. Zhang, Z. Jia, B. Wen, Y. Liu, S. Muraishi, Y. Li, Q. Liu, Acta Mater. **180**, 301 (2019)

[16] W. Ding, X. Zhao, T. Chen, H. Zhang, X. Liu, Y. Cheng, D. Lei, J. Alloys Compd. **830**, 154685 (2020)

[17] S.B. Wang, C.F. Pan, B. Wei, X. Zheng, Y.X. Lai, J.H. Chen, J. Mater. Sci. Technol. **110**, 216 (2022)

[18] H. Jiang, Q. Zheng, Y. Song, Y. Li, S. Li, J. He, L. Zhang, J. Zhao, Mater. Charact. **185**, 111750 (2022)

[19] X. Wu, Z.P. Guan, Z.Z. Yang, X. Wang, F. Qiu, H.Y. Wang, Mater. Sci. Eng. A **869**, 144782 (2023)

[20] M.X. Guo, J. Zhu, Y. Zhang, G.J. Li, T. Lin, J.S. Zhang, L.Z. Zhuang, Mater. Charact. **132**, 248 (2017)

[21] W. Jiang, J. Zhu, G. Li, F. Guan, Y. Yu, Z. Fan, J. Mater. Sci. Technol. **88**, 119 (2021)

[22] X. Liu, Y.L. Ma, X. Wang, S.Y. Zhang, M.X. Zhang, H.Y. Wang, Mater. Sci. Eng. A **872**, 144945 (2023)

[23] Y.J. Shi, Q.L. Pan, M.J. Li, Z.M. Liu, Z.Q. Huang, Trans. Nonferrous Met. Soc. China **25**, 3560 (2015)

[24] T. Radetic, M. Popovic, M. Novakovic, V. Rajic, E. Romhanji, J. Min. Metall. B **59**, 327 (2023)

[25] M. Zhang, D. Wang, H. Nagaumi, R. Wang, X. Zhang, P. Zhou, F. Wu, B. Zhang, Mater. Sci. Eng. A **889**, 145840 (2024)

[26] M. Pourgharibshahi, G. Timelli, Mater. Today Commun. **36**, 106803 (2023)

[27] X. Chen, G. Zhao, G. Liu, L. Sun, L. Chen, C. Zhang, J. Mater. Process. Technol. **275**, 116348 (2020)

[28] K.P. Mingard, B. Roebuck, E.G. Bennett, M.G. Gee, H. Nordenstrom, G. Sweetman, P. Chan, Int. J. Refract. Met. Hard Mater. **27**, 213 (2009)

[29] J. Zhang, S. Han, Y. Sun, X. Chen, P. Chen, Z. Li, G. Huang, F. Pan, Mater. Sci. Eng. A **880**, 145329 (2023)

[30] Z. Zhang, J.H. Zhang, J.S. Xie, S.J. Liu, Y.Y. He, R. Wang, D.Q. Fang, W. Fu, Y.L. Jiao, R.Z. Wu, Mater. Sci. Eng. A **831**, 142259 (2022)

[31] Z. Zhu, M.J. Starink, Mater. Sci. Eng. A **488**, 125 (2008)

[32] Y. Wang, Y. Deng, Q. Dai, K. Jiang, J. Chen, X. Guo, Mater. Sci. Eng. A **803**, 140477 (2021)

[33] J. Zhang, Y. Huang, J. Xiang, G. Huang, X. Chen, H. Zhou, B. Jiang, A. Tang, F. Pan, Mater. Sci. Eng. A **800**, 140320 (2021)

[34] Y. Zhang, J. Jiang, Y. Wang, G. Xiao, Y. Liu, M. Huang, J. Alloys Compd. **893**, 162311 (2022)

[35] G. Fan, G. Wang, H. Choo, P. Liaw, Y. Park, B. Han, E. Lavernia, Scr. Mater. **52**, 929 (2005)

[36] L. Hua, X. Hu, X. Han, Mater. Des. **196**, 109192 (2020)

[37] W. Liu, J. Morris, Metall. Mater. Trans. A **35**, 265 (2004)

[38] H. Xu, L.D. Xu, S.J. Zhang, Q. Han, Scr. Mater. **54**, 2191 (2006)

[39] M. Jin, J. Li, G.J. Shao, Mater. Sci. Forum **546**, 825 (2007)

[40] K. Yoshida, T. Ishizaka, M. Kuroda, S. Ikawa, Acta Mater. **55**, 4499 (2007)

[41] N.Q. Chinh, D. Olasz, A.Q. Ahmed, G. Sáfrán, J. Lendvai, T.G. Langdon, Mater. Sci. Eng. A **862**, 144419 (2023)

[42] W.J.P.X. Wang, S. Esmaeili, D.J. Lloyd, J.D. Embury, Metall. Mater. **34**, 2913 (2003)

[43] R. Li, M. Wang, Z. Li, P. Cao, T. Yuan, H. Zhu, Acta Mater. **193**, 83 (2020)

[44] M. Zha, Y. Li, R.H. Mathiesen, R. Bjørge, H.J. Roven, Acta Mater. **84**, 42 (2015)

[45] S. Esmaeili, D.J. Lloyd, W.J. Poole, Acta Mater. **51**, 2243 (2003)

[46] O.R. Myhr, Ø. Grong, S.J. Andersen, Acta Mater. **49**, 65 (2001)

[47] M.W. Zandbergen, A. Cerezo, G.D.W. Smith, Acta Mater. **101**, 149 (2015)